




How Consumption and Repulsion Set Planetary Gap Depths and the Final Masses of Gas Giants

M. M. Rosenthal¹[★], E. I. Chiang^{2,3}, S. Ginzburg², R. A. Murray-Clay¹

¹ *Department of Astronomy and Astrophysics, University of California, Santa Cruz, CA 95064, USA*

² *Department of Astronomy, University of California at Berkeley, CA 94720, USA*

³ *Department of Earth and Planetary Science, University of California, Berkeley, CA 94720, USA*

Released 16 June 2020

ABSTRACT

Planets open gaps in discs. Gap opening is typically modeled by considering the planetary Lindblad torque which repels disc gas away from the planet’s orbit. But gaps also clear because the planet consumes local material. We present a simple, easy-to-use, analytic framework for calculating how gaps deplete and how the disc’s structure as a whole changes by the combined action of Lindblad repulsion and planetary consumption. The final mass to which a gap-embedded gas giant grows is derived in tandem. The analytics are tested against 1D numerical experiments and calibrated using published multi-dimensional simulations. In viscous alpha discs, the planet, while clearing a gap, initially accretes practically all of the gas that tries to diffuse past, rapidly achieving super-Jupiter if not brown dwarf status. By contrast, in inviscid discs—that may still accrete onto their central stars by, say, magnetized winds—planets open deep, repulsion-dominated gaps. Then only a small fraction of the disc accretion flow is diverted onto the planet, which grows to a fraction of a Jupiter mass. Transitional disc cavities might be cleared by families of such low-mass objects opening inviscid, repulsion-dominated, overlapping gaps which allow most of the outer disc gas to flow unimpeded onto host stars.

Key words: accretion, accretion discs – planets and satellites: formation – planets and satellites: gaseous planets – planets and satellites: physical evolution – planet-disc interactions – protoplanetary discs

1 INTRODUCTION

Annular gaps in protoplanetary discs are often attributed to embedded planets. The interpretation stems from the theory of satellite-disc interactions that successfully predicted the existence of shepherd moons in planetary rings (e.g., [Goldreich & Tremaine 1982](#)). Satellites in rings, and by analogy planets in discs, repel material away from their orbits as the waves they excite at Lindblad resonances dissipate and impart angular momentum to the ambient medium (see also [Goodman & Rafikov 2001](#); [Ginzburg & Sari 2018](#)). The repulsive, gap-forming planetary Lindblad torque competes against the disc’s viscous torque which diffuses material back into the gap.

Most studies of protoplanetary disc gaps concentrate exclusively on the Lindblad and viscous torques (e.g., [Fung et al. 2014](#); [Kanagawa et al. 2015](#); [Zhang et al. 2018](#)) and neglect how gaps can also deepen because embedded planets consume local disc gas. Exceptions include, e.g., [Zhu](#)

[et al. \(2011\)](#), [Dürmann & Kley \(2015, 2017\)](#), and [Muley et al. \(2019\)](#), whose numerical simulations of planet-disc interactions allow for both planetary accretion and planetary torques. Our aim here is to give an elementary and analytic accounting of both effects: to understand, for planets on fixed circular orbits, how Lindblad repulsion and planetary consumption combine to set gap depths. This is a two-way feedback problem—planetary accretion affects the gas density inside the gap, but the density inside the gap determines the rate of planetary accretion ([Ginzburg & Chiang 2019a, 2019b](#)). Accordingly we will calculate how gas giants grow in tandem with their deepening gaps. Much of our analytic framework is the same as that of [Tanigawa & Tanaka \(2016\)](#) and [Tanaka et al. \(2020\)](#), who used it to study nascent planets in viscous discs; we will explore both viscous and inviscid discs.

The problem of planetary accretion within disc gaps is also a global one insofar as a planet can accrete gas that is brought to it from afar, from regions outside the gap. Thus we will stage our calculations within circumstellar discs that transport mass across decades in radius. This opens up

★ E-mail: mmrosent@ucsc.edu

another form of feedback: in feeding the planet, the disc can have its entire surface density profile changed (e.g., [Lubow & D’Angelo 2006](#); [Zhu et al. 2011](#); [Owen 2016](#)).

Our work is organized as follows. In section 2 we describe how Lindblad repulsion and planetary accretion of disc gas (“consumption”) work together to determine gap depths and surface density profiles of viscous circumstellar accretion discs. Our largely analytic considerations are supplemented with simple numerical experiments modeling planet-disc interactions and disc evolution in 1D (orbital radius). In section 2 we fix, for simplicity, the planet mass; in section 3, we allow the planet mass to grow freely and solve the full two-way feedback problem. In section 4, motivated by recent theoretical and observational developments, we consider discs that transport their mass not by viscous diffusion but rather by angular momentum losses from magnetized winds. For such inviscid, wind-driven discs, accretion is not diffusive but purely advective, and embedded planets carve out especially deep gaps in the absence of viscous backflow. We summarize and discuss the implications of our findings on gas giant masses and disc structure, including the structure of transitional discs, in section 5.

A simplified study such as ours will not capture important (and sometimes poorly understood) effects, among them planetary migration (e.g., [Kley & Nelson 2012](#); [Duffell et al. 2014](#); [Dürmann & Kley 2015, 2017](#); [Fung & Chiang 2017](#); [Kanagawa et al. 2018](#); [McNally et al. 2020](#)), eccentricity evolution (both of the planet and the disc; e.g., [Papaloizou et al. 2001](#); [Goldreich & Sari 2003](#); [Kley & Dirksen 2006](#); [Duffell & Chiang 2015](#); [Muley et al. 2019](#)), and the 3D dynamics of circumplanetary discs (e.g., [Fung et al. 2019](#)). Our goal is not so much to be realistic but to acquire some intuition about the interplay of Lindblad repulsion and planetary accretion, and to provide a baseline understanding that can guide the development and interpretation of more sophisticated models. Where possible, we place our results in context with state-of-the-art numerical experiments in the literature (see in particular section 5).

2 VISCOUS DISCS: SURFACE DENSITY PROFILES AT FIXED PLANET MASS

We study how the surface densities of viscous accretion discs are shaped by repulsive planetary Lindblad torques in addition to planetary accretion of disc gas (“consumption”). Section 2.1 contains analytic considerations which are tested numerically in section 2.2. In these sections, while we allow the disc surface density to deplete by consumption, we do not simultaneously allow the planet’s mass to increase. This fixing of the planet’s mass is done for simplicity, to see how the planet affects the disc but not vice versa. In section 3, we free up the planet’s mass and allow two-way feedback between planet and disc.

2.1 Order-of-magnitude scalings

Consider an accreting planet embedded in a viscous disc. From Figure 1 we identify three disc surface densities: Σ_p at the orbital radius of the planet ($r = r_p$), Σ_+ exterior to the planet, and Σ_- interior to the planet. The planet depresses the local surface density because it is both consuming disc

gas and repelling disc gas away by Lindblad torques. Our goal is to estimate the depth of the planet’s gap in relation to the inner and outer discs: Σ_p/Σ_- and Σ_p/Σ_+ . We assume a steady state where the disc has viscously relaxed: given a viscosity ν , the system age t is at least as long as the diffusion time r^2/ν across the disc. In addition, t is at most the planet growth timescale M_p/\dot{M}_p , so that we may consider the planet mass fixed at any given moment.

Mass flows steadily inward at rate \dot{M}_+ from the outer disc. Part of this flow is accreted by the planet at rate \dot{M}_p , with the rest feeding the inner disc which accretes onto the star at rate \dot{M}_- . Dropping numerical pre-factors (these will be restored in later sections), we have

$$\begin{aligned} \dot{M}_+ &= \dot{M}_- + \dot{M}_p \\ \Sigma_+ \nu &\sim \Sigma_- \nu + \dot{M}_p \\ &\sim \Sigma_- \nu + A \Sigma_p. \end{aligned} \quad (1)$$

There are a number of assumptions embedded in these order-of-magnitude statements. For \dot{M}_+ and \dot{M}_- we have substituted standard steady-state expressions for a disc of shear viscosity ν (e.g., [Frank et al. 2002](#)), valid asymptotically at locations far from any mass sink ($|r - r_p| \gtrsim r_p$). At the same time, the locations we are considering in the outer and inner discs are not so far from the planet that we need to account for spatial variations in ν , which may change by order-unity factors over length scale r .

For the planet’s accretion rate, we have assumed in (1) that it scales linearly with the local surface density Σ_p with proportionality constant A :

$$\dot{M}_p = A \Sigma_p. \quad (2)$$

This assumption is satisfied, e.g., by a planet accreting at the Bondi rate (e.g., [Frank et al. 2002](#)):

$$\begin{aligned} \dot{M}_{p,\text{Bondi}} &\sim \rho_p c_s R_B^2 \\ &\sim \frac{\Sigma_p}{H} c_s \left(\frac{GM_p}{c_s^2} \right)^2 \end{aligned} \quad (3)$$

where ρ_p is the disc midplane mass density near the planet, c_s is the disc sound speed, $R_B = GM_p/c_s^2$ is the Bondi radius, $H = c_s/\Omega$ is the disc scale height, Ω is the orbital angular frequency, and G is the gravitational constant. Then

$$A_{\text{Bondi}} \sim \frac{m^2}{h^4} \Omega r^2 \quad (4)$$

where $m \equiv M_p/M_\star$ is the planet-to-star mass ratio, and $h \equiv H/r$ is the disc aspect ratio. [Ginzburg & Chiang \(2019a\)](#), their section 1.1) discusses how Bondi accretion may be valid for “sub-thermal” planets whose masses are less than

$$M_{\text{thermal}} \sim h^3 M_\star \quad (5)$$

the mass for which the Bondi radius R_B , the Hill radius $R_H \sim m^{1/3} r$, and the disc scale height H are all equal. A sub-thermal planet has $R_B < R_H < H$ —its gravitational sphere of influence has radius R_B , set by gravity and thermal pressure—and should accrete at the Bondi rate, isotropically from the all-surrounding disc ([Ginzburg & Chiang 2019a](#); see also fig. 1 of [Tanigawa & Tanaka 2016](#) for evidence supporting the Bondi m^2 scaling, taken from the 3D simulations of [D’Angelo et al. 2003](#)). For a super-thermal planet having $M > M_{\text{thermal}}$, the hierarchy of length scales reverses so that

$R_B > R_H > H$ —the planet’s sphere of influence, now set by gravitational tides at radius R_H , “pops out” of the disc—and arguably the planet accretes in a more 2D fashion, presenting a cross-section of order $R_H H$ to disc gas that shears by at a velocity ΩR_H . The corresponding “Hill rate” for consumption is then

$$\dot{M}_{p,\text{Hill}} \sim \rho_p \times R_H H \times \Omega R_H \sim \Sigma_p R_H^2 \Omega \quad (6)$$

whence

$$A_{\text{Hill}} \sim m^{2/3} \Omega r^2. \quad (7)$$

A Hill-based scaling for consumption is commonly used in 2D disc-planet hydrodynamical simulations (e.g., Zhu et al. 2011; Dürmann & Kley 2015, 2017; Muley et al. 2019). We have assumed in writing the above that the planet masses are large enough for accretion to be hydrodynamically-limited as opposed to cooling-limited (Ginzburg & Chiang 2019a, cf. their fig. 1).

In this paper we will calculate the growth of planets from sub-thermal to super-thermal masses, so will have occasion to use both A_{Bondi} and A_{Hill} . We recognize that the 2D picture motivating our Hill scaling may not be correct; in 3D, meridional flows from gap walls can feed the planet along its poles (Szulágyi et al. 2014; Morbidelli et al. 2014; Fung & Chiang 2016). Relatedly, the disc density scales with height z above the midplane as $\exp[-z^2/(2H^2)]$ (for an isothermal atmosphere), which implies that a considerable fraction of the disc mass resides between $|z| = H$ and $2H$; accordingly, the planet does not pop out of the disc until it is strongly super-thermal, i.e., until m is a large multiple of h^3 (cf. equation 5). An isotropic version of super-thermal accretion controlled by the Hill sphere gives $\dot{M}_{p,\text{Hill,iso}} \sim \rho_p \times R_H^2 \times \Omega R_H$ or $A_{\text{Hill,iso}} \sim m \Omega r^2 / h$. Yet another prescription for accretion is given by Tanigawa & Watanabe (2002): $A_{\text{TW}} \sim m^{4/3} \Omega r^2 / h^2$, an empirical relation based on their 2D numerical simulations (see also Tanigawa & Tanaka 2016). To the extent that these alternative scalings increase with m more steeply than our nominal $A_{\text{Hill}} \propto m^{2/3}$, whatever final super-thermal planet masses we derive should be lower limits (see sections 2.2.1 and 5).

Momentum conservation provides another relation between the surface densities. It is easiest to write down downstream of the planet in the accretion flow (in the inner disc), as the flow of momentum upstream (in the outer disc) is complicated by the mass sink presented by the planet. In the inner disc there are no sinks of mass or momentum, only a steady transmission of mass inward and angular momentum outward (assuming, as we do throughout this paper, a non-migrating planet; see section 5 for pointers to the migrating case). The rate at which angular momentum is carried viscously outward by the inner disc equals the viscous transport rate local to the planet, plus the repulsive Lindblad torque exerted by the planet on the disc:¹

$$\Sigma_- \nu \Omega r^2 \sim \Sigma_p \nu \Omega r^2 + B \Sigma_p \Omega r^2 \quad (8)$$

with

$$B \sim \frac{m^2}{h^3} \Omega r^2 \quad (9)$$

¹ The planet excites waves in the inner disc which carry negative angular momentum inward. This is equivalent to transmitting positive angular momentum outward.

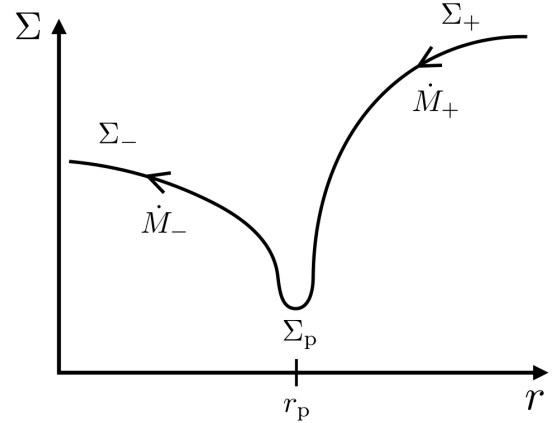


Figure 1. Sketch of the disc surface density and accretion flow in the vicinity of a planet. The planet is located at orbital radius r_p , inside a gap having surface density Σ_p . At $r > r_p$, the disc surface density is Σ_+ and mass accretes inward at rate \dot{M}_+ . Downstream of the planet, at $r < r_p$, the corresponding surface density and accretion rate are Σ_- and \dot{M}_- , respectively. The difference $\dot{M}_+ - \dot{M}_-$ is the accretion rate onto the planet \dot{M}_p .

given by the standard Goldreich & Tremaine (1980) linear Lindblad torque, integrating the effects of all Lindblad resonances up to the torque cutoff. A similar statement to (8), dropping the viscous term local to the planet, was made by Fung et al. (2014). Given B , (8) can be solved for the gap contrast with the inner disc:

$$\frac{\Sigma_p}{\Sigma_-} \sim \frac{1}{1 + B/\nu} \quad (10)$$

(see also Duffell & MacFadyen 2013; Kanagawa et al. 2015; Ginzburg & Sari 2018). Combining mass conservation (1) with momentum conservation (8) yields the gap contrast with the outer disc:

$$\frac{\Sigma_p}{\Sigma_+} \sim \frac{1}{1 + (A + B)/\nu}. \quad (11)$$

An equivalent equation is derived by Tanigawa & Tanaka (2016, their appendix B) and Tanaka et al. (2020, their equation 26). Equations (10) and (11) inform us that planetary consumption ($A \neq 0$) leads to asymmetric gap contrasts: a deeper gap relative to the outer disc than to the inner disc. The outer gap contrast is the more important insofar as the outer disc controls surface densities everywhere downstream; in other words, Σ_+ is the independent variable while Σ_p and Σ_- are dependent variables. Equation (11) states that, given Σ_+ , the effects of accretion (A) and repulsion (B) in setting the gap depth Σ_p are additive (not multiplicative). If $A > B$, then consumption dominates.

For $A = A_{\text{Bondi}}$ and B given by (9),

$$A_{\text{Bondi}}/B \sim 1/h > 1 \quad (12)$$

and consumption dominates repulsion in setting the gap depth, independent of planet mass in the sub-thermal regime. On the other hand, for $A = A_{\text{Hill}}$,

$$A_{\text{Hill}}/B \sim m^{-4/3} h^3 \quad (13)$$

which says that for super-thermal planets that are massive enough, repulsion dominates consumption ($A_{\text{Hill}}/B < 1$).

We may also solve for the relative accretion rates:

$$\frac{\dot{M}_p}{\dot{M}_+} \sim \frac{A\Sigma_p}{\Sigma_+\nu} \sim \frac{A/\nu}{1+(A+B)/\nu} \quad (14)$$

$$\frac{\dot{M}_-}{\dot{M}_+} \sim \frac{\Sigma_-}{\Sigma_+} \sim \frac{1+B/\nu}{1+(A+B)/\nu}. \quad (15)$$

A couple example limiting cases of (14) and (15) are as follows. If we take $A/B = A_{\text{Bondi}}/B \sim 1/h > 1$ and further assume that $B/\nu > 1$ so that the inner gap contrast is significant (equation 10), we find

$$\frac{\dot{M}_p}{\dot{M}_+} \sim 1 - B/A_{\text{Bondi}} \sim 1 - h \quad (16)$$

$$\frac{\dot{M}_-}{\dot{M}_+} \sim B/A_{\text{Bondi}} \sim h \quad (17)$$

which says that the planet consumes nearly all of the mass supplied to it by the outer disc, leaving behind a fraction h to feed the inner disc. If instead we take $A/B = A_{\text{Hill}}/B$ and further assume $B > A_{\text{Hill}} > \nu$ (repulsion-limited and deep gap), then

$$\frac{\dot{M}_p}{\dot{M}_+} \sim A_{\text{Hill}}/B \sim m^{-4/3}h^3 < 1 \quad (18)$$

$$\frac{\dot{M}_-}{\dot{M}_+} \sim 1 - A_{\text{Hill}}/B \sim 1 - m^{-4/3}h^3 \quad (19)$$

and the planet diverts only a small fraction, A_{Hill}/B , of the disc accretion flow onto itself.

The order-of-magnitude considerations presented here are firmed up in subsequent sections, including in Appendix A, where we derive in greater analytic detail the surface density profile and mass accretion rates, drawing from [Lubow & D’Angelo \(2006\)](#).

2.2 Numerical simulations

2.2.1 Procedure

We solve numerically for the 1D evolution of a viscously shearing disc (e.g., [Frank et al. 2002](#)) with a planetary mass sink. The governing equation for the surface density $\Sigma(r, t)$ in cylindrical radius r and time t reads

$$\frac{\partial \Sigma}{\partial t} = \frac{3}{r} \frac{\partial}{\partial r} \left[r^{1/2} \frac{\partial}{\partial r} (r^{1/2} \nu \Sigma) \right] - \frac{\dot{M}_p(t)}{2\pi r} \delta(r - r_p) \quad (20)$$

where δ is the Dirac delta function and r_p is the radial position of the planet (held fixed). For the viscosity ν we employ the [Shakura & Sunyaev \(1973\)](#) α -prescription:

$$\nu = \alpha c_s^2 / \Omega = \alpha h^2 \Omega r^2 \quad (21)$$

where Ω is the Keplerian orbital frequency around a $1 M_\odot$ star, $c_s = \sqrt{k_B T / \bar{m}}$, the disc temperature is $T = 200 \text{ K}(r/\text{au})^{-1/2}$, k_B is Boltzmann’s constant, $\bar{m} = 2m_H$ is the mean molecular mass, m_H is the mass of the hydrogen atom, and

$$h \equiv H/r = c_s / (\Omega r) \approx 0.054 \left(\frac{r}{10 \text{ au}} \right)^{1/4}. \quad (22)$$

We fix $\alpha = 10^{-3}$ for the results in this section. Given these inputs, $\nu = \nu(r) \propto r^1$.

Apart from the mass sink, equation (20), which combines the 1D mass and momentum equations, is identical to

the diffusion equation governing an isolated viscous disc as derived by [Lynden-Bell & Pringle \(1974\)](#). What is missing is an explicit accounting for the repulsive Lindblad torque exerted by the planet. Many studies include the planetary torque by introducing, into the momentum equation, a term for the torque per unit radius that scales as $\text{sgn}(x)/x^4$, where $x \equiv r - r_p$ (e.g., [Lin & Papaloizou 1986](#); [Lubow & D’Angelo 2006](#)). Compared against 2D hydrodynamical simulations, this $1/x^4$ prescription has been shown in 1D studies to reproduce the azimuthally averaged surface density profiles of repulsive gaps near their peripheries (at $x \gtrsim 4H$) but not near gap centers (at $x \lesssim 4H$; [Fung et al. 2014](#), their section 4.3). In particular the 1D torque density prescription, which assumes angular momentum is deposited locally and neglects wave propagation, fails to recover the flat bottoms of gaps and the surface densities there (cf. [Ginzburg & Sari 2018](#) who use the [Goodman & Rafikov 2001](#) wave steepening theory to lift these assumptions). This shortcoming of the $1/x^4$ prescription means that it cannot be used to compute the planetary accretion rate \dot{M}_p , which depends on knowing the gas density in the planet’s immediate vicinity.

What we do instead to include the repulsive Lindblad torque when calculating planetary accretion is as follows. Within the radial grid cell at $r = r_p$ of width Δr_p , the surface density is reduced after every timestep Δt according to

$$\Sigma(r_p, t + \Delta t) = \Sigma(r_p, t) - \frac{\dot{M}_p(t)\Delta t}{2\pi r_p \Delta r_p} \quad (\text{simulation}) \quad (23)$$

where the label “simulation” reminds us that this equation applies to the numerical simulation only and should not be used outside of that context. It is in evaluating \dot{M}_p that we include, in a “sub-grid” manner, the repulsive Lindblad gap:

$$\dot{M}_p(t) = A \times \frac{\Sigma(r_p, t)}{1 + B/\nu} \quad (\text{simulation}). \quad (24)$$

What equation (24) says is that the disc surface density the planet actually “sees” when consuming local gas is lower than the numerically computed “grid-level” surface density $\Sigma(r_p, t)$ —lower by the Lindblad reduction factor $1/(1 + B/\nu)$ (equation 10). In other words, repulsion is encoded/enforced at a sub-grid level. We stress that equation (24) is used only in our numerical simulation to capture repulsion and should not be used outside of it; contrast (24) with, e.g., (14), and note that $\Sigma(r_p, t)$ is notation specific to the simulation and should not be confused with Σ_p , the actual surface density at the planet’s position.

Our numerical procedure captures the gap depth but not the gap width, as the sub-grid modification is restricted (for simplicity) to the grid cell containing the planet. We consider this crude scheme acceptable insofar as we are more interested in the gross magnitudes for Σ_p/Σ_+ and Σ_p/Σ_- and less interested in the precise surface density gradients. An untested assumption underlying our numerical procedure—and in our steady-state analytics—is that material flows radially through the gap at whatever velocity u_r is needed to maintain continuity, i.e., to enforce $\dot{M}_- = \dot{M}_+ - \dot{M}_p = -2\pi \Sigma_p r_p u_r$ (where $u_r < 0$ for accretion toward the star). We cannot test this assumption as we do not resolve the flow dynamics inside the gap. We will call out this assumption in the results to follow (sections 3.1 and 4.4). Also, as a reminder, we note that while the surface density changes as a result of consumption, in this subsection we fix \dot{M}_p , i.e., we

do not update M_p using \dot{M}_p (this assumption is relaxed in section 3).

In evaluating the consumption and repulsion coefficients A and B , we make choices similar to those in our earlier order-of-magnitude analysis (section 2.1), except that now we include numerical pre-factors for greater precision:

$$A_{\text{Bondi}} = 0.5 \Omega r^2 \frac{m^2}{h^4} \quad \text{for sub-thermal } m \leq 3h^3 \quad (25)$$

$$A_{\text{Hill}} = 2.2 \Omega r^2 m^{2/3} \quad \text{for super-thermal } m > 3h^3 \quad (26)$$

$$B = 0.04 \Omega r^2 \frac{m^2}{h^3} \quad (27)$$

where all quantities are evaluated at r_p . The pre-factor of 0.5 in equation (25) is calibrated using 3D simulation results for \dot{M}_p from D'Angelo et al. (2003; these are re-printed in fig. 1 of Tanigawa & Tanaka 2016). The coefficient of 2.2 in equation (26) follows from requiring that (25) match (26) at the thermal mass

$$M_{\text{thermal}} \equiv 3h^3 M_\star \simeq 0.5 \left(\frac{h}{0.054} \right)^3 M_J \quad (28)$$

defined by equating H with $R_H = (m/3)^{1/3} r$, with M_J the mass of Jupiter. Equation (27) is taken from the numerical 2D simulations of Kanagawa et al. (2015, see also Duffell & MacFadyen 2013 and Duffell 2015 who report similar results).

Note further that the expressions we used in section 2.1 for the steady disc accretion rates \dot{M}_+ and \dot{M}_- should be amended with the numerical pre-factor 3π , i.e., $\dot{M}_+ = 3\pi \Sigma_+ \nu$ and similarly for \dot{M}_- (e.g., Frank et al. 2002). This correction is already embedded in the diffusion equation (20). Including this pre-factor in equation (1) implies that A should be replaced with $A/(3\pi)$ in equations (11)–(19). Putting it all together, we have

$$\frac{A_{\text{Bondi}}}{3\pi B} \simeq \frac{1.3}{h} > 1 \quad (29)$$

implying that consumption always dominates for sub-thermal masses. Furthermore,

$$\frac{A_{\text{Hill}}}{3\pi B} \simeq 5.5 m^{-4/3} h^3 \simeq 1.0 \left(\frac{m}{5 \times 10^{-3}} \right)^{-4/3} \left(\frac{h}{0.054} \right)^3 \quad (30)$$

implying that repulsion dominates for super-thermal masses exceeding a ‘‘repulsion mass’’

$$\begin{aligned} M_{\text{repulsion,visc}} &\simeq 3.6 h^{9/4} M_\star \\ &\simeq 5.3 M_J \left(\frac{h}{0.054} \right)^{9/4} \simeq 5.3 M_J \left(\frac{r}{10 \text{ au}} \right)^{9/16} \\ &\simeq 1.2 h^{-3/4} M_{\text{thermal}} \simeq 11 \left(\frac{0.054}{h} \right)^{3/4} M_{\text{thermal}}. \end{aligned} \quad (31)$$

For $M < M_{\text{repulsion,visc}}$, consumption dominates and the planet accretes nearly all the disc gas that tries to diffuse past; for $M > M_{\text{repulsion,visc}}$, repulsion dominates and the planet’s accretion rate falls below the disc accretion rate. The above expression for $M_{\text{repulsion,visc}}$ depends on our assumption that planetary accretion follows our Hill scaling $A_{\text{Hill}} \propto m^{2/3}$ for super-thermal masses. As discussed in section 2.1, this assumption might not be correct. If instead of

A_{Hill} we use $A_{\text{TW}} = 0.29 \Omega r^2 m^{4/3} / h^2$ as found from the 2D numerical simulations of Tanigawa & Watanabe (2002), we would find $A_{\text{TW}}/(3\pi B) \simeq 4 (M_p/M_J)^{-2/3} (h/0.054)$, in which case the mass above which repulsion dominates would change to $M_{\text{repulsion,visc,TW}} \simeq 9 M_J [r/(10 \text{ au})]^{3/8}$. This is nearly twice the value of $M_{\text{repulsion,visc}}$ given by (31), and would imply a more extended consumption-dominated growth phase. Insofar as our nominal model adopts A_{Hill} which leads to a more limited consumption-dominated growth phase, the planet masses we compute for our viscous disc model are lower limits.

So far we have described how we compute the mass sink term, which includes the sub-grid Lindblad torque, in equation (20). The remaining diffusive term is solved in a standard way. We first change variables to $z \equiv r^{1/2} \nu \Sigma$ and $y \equiv 2r^{1/2}$ so that the diffusive portion of equation (20) reads

$$\frac{\partial z}{\partial t} = \frac{12\nu}{y^2} \frac{\partial^2 z}{\partial y^2} \quad (32)$$

with non-constant diffusion coefficient $12\nu/y^2$. We solve equation (32) as an initial value problem using an implicit scheme (e.g., Press et al. 2007). Our computation grid extends from an inner boundary of $r_{\text{in}} = 0.01 \text{ au}$ to an outer boundary of $r_{\text{out}} = 500 \text{ au}$, and is divided into 300 cells that are uniform in Δy . We fix the timestep $\Delta t = 10^{-4} t_{\nu,p}$, where $t_{\nu,p} \equiv r_p^2/\nu(r_p) \simeq 1.7 \text{ Myr}$ is the viscous diffusion timescale at the planet’s orbital radius of $r_p = 10 \text{ au}$ (where $h \simeq 0.054$). Recognizing that our transformed variable z is proportional to the viscous torque $2\pi\nu\Sigma r^3 d\Omega/dr \propto r^{1/2}\nu\Sigma$, we use a torque-free inner boundary condition, $z(r_{\text{in}}) = 0$, as would be the case if the disc were truncated by a co-rotating stellar magnetosphere (shearless boundary layer). At the outer boundary we assume the torque gradient $\partial z/\partial r(r_{\text{out}}) = 0$. Neither boundary condition is critical as we are interested in the flow near the planet, away from either boundary.

The surface density of the disc is initialized with the similarity solution for an isolated viscous accretion disc with $\nu \propto r^1$ (Lynden-Bell & Pringle 1974; Hartmann et al. 1998):

$$\Sigma(r, 0) = \frac{M_{\text{disc}}}{2\pi r_1^2} \frac{r_1}{r} e^{-r/r_1} \quad (\text{simulation}) \quad (33)$$

where $M_{\text{disc}} = 15.5 M_J \simeq 0.015 M_\odot$ is the initial mass of the disc and $r_1 = 30 \text{ au}$ is a characteristic disc radius (where the diffusion time is $r_1^2/\nu \simeq 5 \text{ Myr}$). We consider two fixed planet masses, $M_p = 0.3 M_J < M_{\text{thermal}}$ and $M_p = 10 M_J > M_{\text{thermal}}$. Planet masses that freely grow are modeled in section 3.

At every timestep, we first advance $\Sigma(r, t) \rightarrow \Sigma(r, t + \Delta t)$ for all r according to (32) using the implicit solver, and then we advance $\Sigma(r_p, t) \rightarrow \Sigma(r_p, t + \Delta t)$ using (23) and (24). This procedure is repeated until the disc is evolved for several $t_{\nu,p}$, long enough for the disc near the planet to achieve a quasi-steady state.

2.2.2 Results

Figure 2 shows, for $M_p = \{0.3, 10\} M_J$, the numerically computed surface density profiles $\Sigma(r)$ at $t = 3t_{\nu,p} \simeq 5 \text{ Myr}$. Overlaid for comparison is our numerical solution without a planet, which we have verified matches the analytic time-dependent similarity solution of Lynden-Bell & Pringle (1974). For the case with a planet, rather than plot at

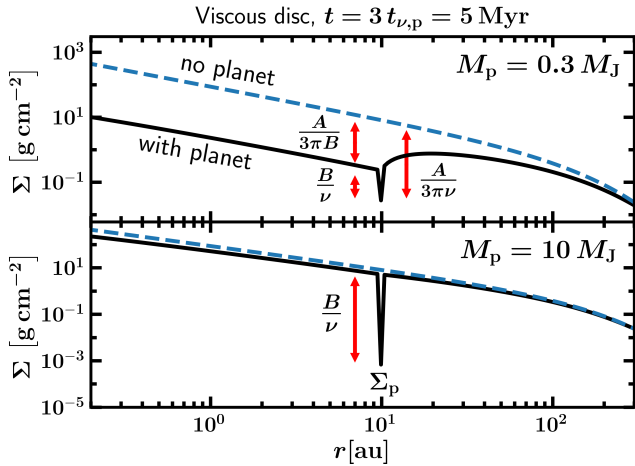


Figure 2. How the surface density profile of a viscous disc responds to a planet that both consumes disc gas, and repels gas away by Lindblad torques. Surface densities are calculated from our 1D numerical simulation of a planet of fixed mass, either $M_p = 0.3 M_J$ (top panel) or $M_p = 10 M_J$ (bottom panel), at $t = 3 t_{\nu,p}$ when the disc near the planet at $r_p = 10$ au has viscously relaxed. When computing the planetary accretion rate \dot{M}_p , the gap is modeled as a single cell whose “true” surface density equals the grid-level Σ lowered by a factor of $(1 + B/\nu) \approx B/\nu$; plotted here are the true sub-grid values Σ_p . Accordingly, the planet’s gap is not spatially resolved and its width should not be taken literally from this figure. Red double-tipped arrows have lengths equal to their associated variables in dex, and demonstrate good agreement between numerics and analytics. The planet of mass $M_p = 0.3 M_J$, accreting at the Bondi rate, creates an asymmetric gap, with the inner disc surface density Σ_- lower than the outer Σ_+ by $A_{\text{Bondi}}/(3\pi B) > 1$; conditions are always consumption-dominated for Bondi accretion and B as given by (27). The planet of mass $M_p = 10 M_J$, accreting at the Hill rate, creates a symmetric gap where $\Sigma_-/\Sigma_+ \sim 1$; conditions here are repulsion-dominated as $M_p > M_{\text{repulsion,visc}}$ (equation 31).

face value the numerically computed (grid-level) $\Sigma(r_p, t)$, we plot that value multiplied by the sub-grid reduction factor $1/(1 + B/\nu)$ —this is the “true” value for Σ_p that incorporates the repulsive Lindblad torque. Since this sub-grid correction factor is applied to only a single grid point, we cannot resolve gap widths; our focus instead is on the gross gap contrasts Σ_p/Σ_+ and Σ_p/Σ_- .

The surface density profiles shown in Figure 2 conform to the analytic considerations of section 2.1. For $M_p = 0.3 M_J$ (top panel), conditions are consumption-limited: $\Sigma_+/\Sigma_p \sim A_{\text{Bondi}}/(3\pi\nu)$ (equation 11 in the limit $A_{\text{Bondi}}/(3\pi) > B > \nu$) and the surface density of the entire interior disc is depressed relative to the same disc without a planet by a factor of $\Sigma_+/\Sigma_- \sim \dot{M}_+/\dot{M}_- \approx A_{\text{Bondi}}/(3\pi B)$ (equations 15 and 17). By comparison, for $M_p = 10 M_J$ (bottom panel), the gap is more nearly symmetric, $\Sigma_+/\Sigma_- \sim 1$ (equations 15 and 19), and deep and repulsion-dominated, $\Sigma_+/\Sigma_p \sim B/\nu$ (equation 11 in the limit $B > A_{\text{Hill}}/(3\pi) > \nu$).

So long as consumption is stronger than repulsion in the sense that $A/(3\pi) > B$ —a condition that we have shown always obtains for sub-thermal masses accreting at the Bondi rate, and for sufficiently low-mass super-thermal masses accreting at the Hill rate ($M < M_{\text{repulsion,visc}}$)—repulsion does

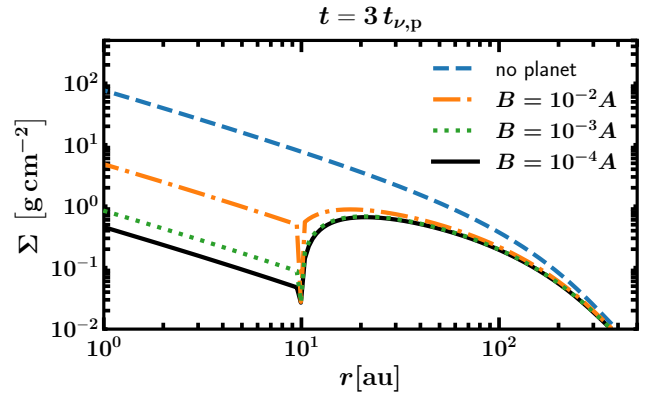


Figure 3. Same as Figure 2 for the case $M_p = 0.3 M_J$, but for different choices of B scaled to A_{Bondi} . As long as $A_{\text{Bondi}}/(3\pi) > B$, the planet’s gap is consumption-dominated and its surface density Σ_p is independent of the repulsion coefficient B . The depression of the inner disc relative to the outer disc is, however, sensitive to B for $B > \nu$; $\Sigma_-/\Sigma_+ \approx (1 + B/\nu)/[A_{\text{Bondi}}/(3\pi\nu)]$.

not much affect the gap surface density Σ_p . Figure 3 demonstrates that different choices for the repulsion coefficient $B = \{10^{-2}, 10^{-3}, 10^{-4}\} \times A_{\text{Bondi}}$ all yield practically the same Σ_p (when corrected to the true sub-grid value) relative to Σ_+ . What repulsion, in combination with consumption, affects instead is how much gas leaks past the planet into the inner disc: the three different values for B in Figure 3 yield three inner disc surface densities that, from equation (15), scale as $\Sigma_-/\Sigma_+ \approx (1 + B/\nu)/[1 + A_{\text{Bondi}}/(3\pi\nu)]$. This factor scales as $3\pi B/A_{\text{Bondi}}$ when $A_{\text{Bondi}}/(3\pi) > B > \nu$ (dot-dashed and dotted lines), and as $1/[1 + A_{\text{Bondi}}/(3\pi\nu)]$ when $B < \nu$ (solid line; in this limit repulsion has no effect).

3 VISCIOUS DISCS: GAS GIANT GROWTH

3.1 Numerical calculation at $r_p = 10$ au

We now relax the assumption that the planet mass remains fixed, and at every timestep update M_p according to \dot{M}_p computed using equation (24). Our numerical procedure is unchanged from section 2.2 except that we initialize the planet mass at $M_p(0) = 0.1 M_J$ and allow it to grow. For our nominal disc parameters ($\alpha = 10^{-3}$, $h = 0.054$ at $r_p = 10$ au), a starting planet mass of $0.1 M_J$ ($m \approx 0.95 \times 10^{-4}$) implies that, initially, $A = A_{\text{Bondi}}$, $A_{\text{Bondi}}/(3\pi B) \approx 1.3/h \approx 24$ (a consumption-dominated gap), $A_{\text{Bondi}}/(3\pi\nu) \approx 19$ (a strong outer gap contrast), and $B/\nu \approx 0.79$ (a weak inner gap contrast).

Figure 4 shows two snapshots in time of $\Sigma(r)$ and the disc mass flow rate $\dot{M}_{\text{disc}}(r) = -2\pi r u_r$, where

$$u_r = -\frac{3}{\Sigma r^{1/2}} \frac{\partial}{\partial r} \left(\nu \Sigma r^{1/2} \right) \quad (34)$$

is the gas radial velocity (e.g., Frank et al. 2002) evaluated numerically from our solution for Σ (omitting the single-point discontinuity at $r = r_p$). Note that $\dot{M}_{\text{disc}} > 0$ indicates inward mass transport, toward the star. The planet accretes predominantly from the outer disc, notwithstanding a small contribution from the inner disc before the disc

has viscously relaxed; this early-time contribution can be seen at $t = 0.3 t_{v,p}$ when $\dot{M}_{\text{disc}} < 0$ from $r \sim 3$ au to the planet’s orbit. The behaviour of \dot{M}_{disc} at $r \sim 100$ au is characteristic of a viscous disc near its turn-around “transition radius” (Lynden-Bell & Pringle 1974; Hartmann et al. 1998), outside of which the disc has not yet viscously relaxed; this outermost disc behaviour is not caused by the planet.

Embedded in Figure 4 is our assumption, first mentioned in section 2.2.1, that the disc flow inside the gap maintains continuity. At $t = 3 t_{v,p}$, $\dot{M}_{\text{disc}}(r > r_p)$ is, to within a factor of 2, the same as $\dot{M}_{\text{disc}}(r < r_p)$. Because the gap surface density Σ_p at this time is about 4 orders of magnitude smaller than the surface densities Σ_+ and Σ_- outside the gap, the radial velocity $|u_r|$ within the gap must be 4 orders of magnitude larger than the radial velocities outside, to maintain the near-constancy of \dot{M}_{disc} across r_p . Since the radial accretion velocities away from the gap are of order $r/t_v \sim v/r \sim \alpha h c_s \sim 2$ cm/s, we must have $|u_r| \sim 0.2$ km/s within the gap. How such a radial velocity is achieved is not specified by our model, which does not resolve the gap spatially.

Figure 5 displays the planet’s mass as a function of time. We identify a consumption-dominated phase during which the planet grows from 0.1 to $5 M_J$ ($M < M_{\text{repulsion,visc}}$; equation 31) and a slower repulsion-dominated phase between 5 and $8 M_J$ ($M > M_{\text{repulsion,visc}}$). During the first phase, accretion starts at the Bondi rate and switches to the Hill rate once $M_p > M_{\text{thermal}} \simeq 0.5 M_J$ (equations 28 and 25–26). A consumption-dominated ($A/(3\pi) > B$) and deep ($A/(3\pi) > \nu$) gap implies from (14) that $\dot{M}_p \simeq \dot{M}_+$, i.e., the planet’s accretion rate is about as large as it can be. During the final repulsion-limited phase, when $M_p > 5 M_J$ and $A_{\text{Hill}}/(3\pi) > B$, consumption slows and the planet undergoes a last near-doubling in mass as the remainder of the disc diffuses away, onto the star.

3.2 Analytic estimates of the final planet mass

We can compare our numerical result for the final mass at $r_p = 10$ au to the following analytic estimates, derived by neglecting the initial short-lived Bondi accretion phase and assuming that at all times the planet accretes at the Hill rate ($A = A_{\text{Hill}}$) and has a large inner gap contrast ($B > \nu$):

$$\begin{aligned} \dot{m} &= \frac{A_{\text{Hill}} \Sigma_p}{M_\star} \\ &= \frac{A_{\text{Hill}}}{M_\star} \frac{\Sigma_+ \nu}{A_{\text{Hill}}/(3\pi) + B} \end{aligned} \quad (35)$$

where we have used (11). At small orbital distances, final planet masses exceed $M_{\text{repulsion,visc}}$ and so their final growth phase is repulsion-limited:

$$\begin{aligned} \dot{m} &= \frac{A_{\text{Hill}}}{B} \frac{\Sigma_+ \nu}{M_\star} \\ &= 55 \alpha h^5 m^{-4/3} \frac{\Sigma_+ r_p^2}{M_\star} \Omega. \end{aligned} \quad (36)$$

We approximate Σ_+ using the similarity solution for an isolated viscous disc with no planet and $\nu \propto r^1$:

$$\Sigma_+ \sim \frac{M_{\text{disc}}}{2\pi r_1^2} \left(\frac{r_1}{r_p} \right) T^{-3/2} e^{-(r_p/r_1)/T} \quad (37)$$

where $T \equiv 1+t/t_1$, $t_1 \equiv r_1^2/[3\nu(r_1)]$, and M_{disc} is the initial disc mass (Lynden-Bell & Pringle 1974; Hartmann et al. 1998). Integrating equation (36) from $t = 0$ to t gives

$$\begin{aligned} m(t) &\sim \left(\frac{385}{18\sqrt{\pi}} \frac{M_{\text{disc}} h^5 r_1}{M_\star h_1^2 r_p} \right)^{3/7} \\ &\times \left[\text{Erf} \left(\sqrt{\frac{r_p}{r_1}} \right) - \text{Erf} \left(\sqrt{\frac{r_p t_1}{r_1(t+t_1)}} \right) \right]^{3/7} \quad (\text{repulsion-limited}) \end{aligned} \quad (38)$$

where h_1 is the disc aspect ratio at r_1 . As $t \rightarrow \infty$, equation (38) simplifies to

$$m_{\text{final,visc}} \sim \left[\frac{385}{18\sqrt{\pi}} \frac{M_{\text{disc}} h^5 r_1}{M_\star h_1^2 r_p} \text{Erf} \left(\sqrt{\frac{r_p}{r_1}} \right) \right]^{3/7} \quad (\text{repulsion-limited}) \quad (39)$$

which further simplifies in the limit $r_p \ll r_1$ (away from the initial disc outer edge) to

$$M_{\text{final,visc}} \sim 10 M_J \left(\frac{M_{\text{disc}}}{15.5 M_J} \right)^{3/7} \left(\frac{r_p}{10 \text{ au}} \right)^{9/28} \quad (\text{repulsion-limited}) \quad (40)$$

for our fiducial parameters. Note that $M_{\text{final,visc}}$ in these limits is independent of α and r_1 . Equation (40) may be reproduced to order-of-magnitude by multiplying \dot{m} (evaluated at $t = t_1$) by t_1 . In Figure 5 we plot equation (39) as the uppermost horizontal dashed line, labeled $M_{\text{final,visc}}$.

At the largest orbital distances, conditions tend to remain consumption-limited as M_p stays below $M_{\text{repulsion,visc}}$. Then the planet accretes nearly all of the disc gas that tries to diffuse past the planet—and diffusion can be in the outward direction ($\dot{M}_{\text{disc}} < 0$) if the planet is located near or beyond the disc’s turn-around radius. Accordingly we estimate the planet mass as

$$M_p(t) \sim \int_0^t |\dot{M}_{\text{disc}}| dt \quad (\text{consumption-limited}) \quad (41)$$

where \dot{M}_{disc} is approximated by the no-planet similarity solution (equation 35 of Hartmann et al. 1998). For $r_p \leq r_1/2$,

$$M_p(t) \sim M_{\text{disc}} \left(e^{-r_p/r_1} - \frac{e^{-(r_p/r_1)/T}}{\sqrt{T}} \right) \quad (\text{consumption-limited}) \quad (42)$$

and for $r_p > r_1/2$,

$$M_p(t) \sim M_{\text{disc}} \left(\sqrt{\frac{2r_1}{r_p}} e^{-1/2} - e^{-r_p/r_1} - \frac{e^{-(r_p/r_1)/T}}{\sqrt{T}} \right) \quad (\text{consumption-limited}). \quad (43)$$

We will make use of equations (38), (42), and (43) in section 5 when we discuss, in the context of observations, how the final planet mass depends on disc mass and orbital distance.

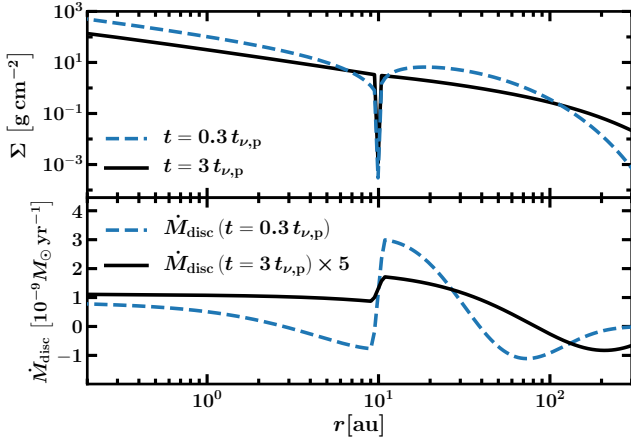


Figure 4. Snapshots of the surface density profile $\Sigma(r)$ and disc accretion rate $\dot{M}_{\text{disc}}(r) = -2\pi\Sigma u_r r$ (> 0 for accretion toward the star) for a planet embedded at $r_p = 10$ au in a viscous $\alpha = 10^{-3}$ disc. The planet mass is allowed to freely grow starting from $M_p(0) = 0.1M_J$. At $t = 0.3t_{\nu,p}$, the planet resides in a consumption-dominated, asymmetric gap (top panel, dashed curve) and accretes from regions both exterior and interior to its orbit which have not yet viscously relaxed (bottom panel, dashed curve). At the later time $t = 3t_{\nu,p}$, the planet has grown sufficiently (see also Figure 5) that its gap is now repulsion-dominated and more symmetric (top panel, solid curve); the planet now accretes only from the outer disc, reducing the flow of mass into the inner disc by less than a factor of 2 (bottom panel, solid curve). At this time we have multiplied \dot{M}_{disc} by a factor of 5 for easier viewing.

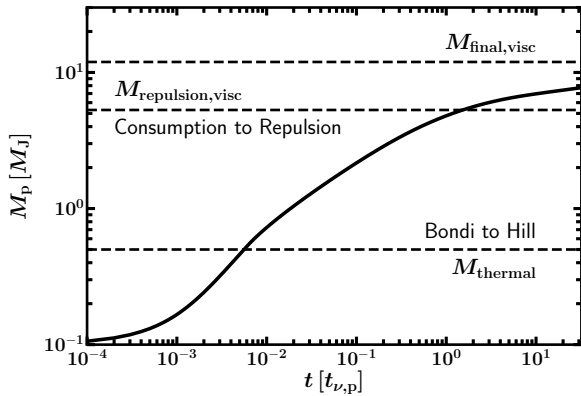


Figure 5. Accretion history of a planet of initial mass $M_p(0) = 0.1M_J$ embedded at $r_p = 10$ au (where $h = 0.054$) in a viscous disc of initial mass $M_{\text{disc}} = 15.5M_J$. Transitions from Bondi accretion to Hill accretion (M_{thermal} , equations 25–26 and 28), and from consumption to repulsion-dominated gaps ($M_{\text{replu,visc}}$, equation 31), are indicated. An analytic estimate of the final planet mass is plotted as $M_{\text{final,visc}}$ (equation 39), computed assuming repulsion-dominated conditions (at $r_p = 10$ au for this disc mass, conditions are actually intermediate between the repulsion and consumption limits, and so plotting equation 42 which assumes consumption-dominated conditions would give a similar result as equation 39; see also Figure 9).

4 PLANETS IN INVISCID WIND-DRIVEN DISCS

Motivated by recent ALMA observations that point to little or no turbulence in protoplanetary discs (e.g., Pinte et al. 2016; Flaherty et al. 2017), and by theoretical work arguing that discs are, for the most part, laminar because they are too cold and dusty to support magnetorotational turbulence (e.g., Gammie 1996; Perez-Becker & Chiang 2011; Bai 2011), we here turn away from the α -based picture of turbulent and diffusive discs, and consider instead inviscid (zero viscosity) discs that accrete by virtue of magnetized winds (e.g., Bai et al. 2016; Bai 2016). We review how wind-driven discs work in section 4.1 and how planets open repulsive gaps in inviscid discs in section 4.2. We then study how repulsion combines with consumption to set gap depths and planetary accretion rates, analytically in section 4.3 and numerically in section 4.4.

4.1 Wind-driven accretion discs

Inviscid, wind-driven accretion discs do not behave diffusively. Instead they are governed by simple advection: at every radius r , material moves inward with a vertically-averaged radial speed u_r because it has lost angular momentum to a magnetized wind. The mass carried away by the wind itself is small compared to the mass advected inward through the disc (see Appendix B, in particular the discussion below equation B5). Then from continuity, including our planetary mass sink,

$$\frac{\partial \Sigma}{\partial t} = \frac{1}{r} \frac{\partial}{\partial r} (\Sigma r u_r) - \frac{\dot{M}_p(t)}{2\pi r} \delta(r - r_p). \quad (44)$$

In Appendix B we show how a wind-driven disc inspired by Bai et al. (2016) and Bai (2016) can have u_r approximately constant (< 0 for accretion). We utilize here, for simplicity, a constant $u_r \equiv c < 0$ model:

$$\frac{\partial \Sigma}{\partial t} = \frac{c}{r} \frac{\partial}{\partial r} (\Sigma r) - \frac{\dot{M}_p(t)}{2\pi r} \delta(r - r_p). \quad (45)$$

It is instructive to examine the solution to (45) when $\dot{M}_p = 0$. The no-planet solution is separable:

$$\Sigma(r, t) = f(r)g(t) = \frac{M_{\text{disc}}}{2\pi(ct_{\text{adv}})^2} \frac{|c|t_{\text{adv}}}{r} e^{-r/(|c|t_{\text{adv}})} e^{-t/t_{\text{adv}}} \quad (46)$$

for constants M_{disc} (the initial disc mass) and t_{adv} , which we interpret as a disc radial advection time or drain-out time. For $c = -4$ cm/s (a value we relate to magnetic field parameters in Appendix B) and $t_{\text{adv}} = 3$ Myr, the characteristic disc size is $|c|t_{\text{adv}} \approx 25$ AU, which seems reasonable. Equation (46) resembles the Lynden-Bell & Pringle (1974) solution for a viscous disc which gives, for $\nu \propto r^1$, a surface density profile that scales as $r^{-1} \exp(-r/r_1)$ at fixed t (equation 37). This spatial resemblance is not surprising, as our viscous disc happens also to have an accretion velocity that is constant with radius: $|u_r| \sim r/t_\nu \sim \nu/r = \text{constant}$. However, the solutions differ in their time behaviours; at fixed r , the wind-driven surface density decays exponentially as $\exp(-t/t_{\text{adv}})$, whereas our viscous disc decays as a power law $t^{-3/2}$ (within viscously relaxed regions at small radii; Lynden-Bell & Pringle 1974; Hartmann et al. 1998). Viscous discs evolve more slowly because they conserve their

total angular momentum; they can only drain away on the inside by redistributing their angular momentum to the outside in a kind of zero-sum game. Wind-driven discs are not so constrained; they lose their angular momentum wholesale to a wind, and so can dissipate more quickly.

We emphasize that $u_r = c$ is a vertically averaged, mass weighted, radial accretion velocity. In simulations by [Bai & Stone \(2013\)](#) of discs whose magneto-thermal winds are anchored at their electrically conductive surfaces, accretion actually occurs in a vertically thin, rarefied layer several scale heights above the midplane. The radial accretion velocity in this high-altitude layer is fast, on the order of the sound speed c_s . The bulk of the mass of the disc, below this layer, is inert (see fig. 10 of [Bai & Stone 2013](#)). It is with this static and inviscid gas, extending from the midplane to a couple scale heights above and below, that the planet interacts, as we now describe.

4.2 Repulsion in inviscid discs

Without viscosity, disc gas in the vicinity of the planet depletes indefinitely, as it is repelled by the planetary Lindblad torque but cannot diffuse back. Under these conditions, [Ginzburg & Chiang \(2019a\)](#) derived how the gas density at the center of the planet's gap scales with elapsed time t , for a given planet-to-star mass ratio $m = M_p/M_\star$ and disc aspect ratio $h = H/r$ (see the inviscid branch of their equation 17, and also their appendix):

$$\frac{\Sigma_p}{\Sigma_-} \sim h^{549/49} m^{-4} (\Omega t)^{-39/49} \equiv \tilde{B}_{\text{inv}}^{-1} \quad (47)$$

where Ω is the orbital frequency of the planet, Σ_p is the surface density within the gap, and Σ_- is the surface density downstream of the planet in the accretion flow (see Figure 1). By construction, t is the time over which the planet's mass is close to its given value m (say within a factor of 2). In practice, for inviscid discs where gaps deepen dramatically with increasing planet mass, the mass doubling time of a planet lengthens with each doubling, so t is of order the system age.

Equation (47) does not apply when $\tilde{B}_{\text{inv}} < 1$, i.e., when a repulsive gap has not yet been opened because not enough time has elapsed for a given planet mass. To account for this possibility, we generalize (47) using

$$\frac{\Sigma_p}{\Sigma_-} \sim \frac{1}{1 + \tilde{B}_{\text{inv}}} \quad (48)$$

by analogy with equation (10) for the viscous case. Note that \tilde{B}_{inv} is dimensionless while its viscous counterpart B has dimensions of viscosity.

4.3 Consumption and repulsion combined

We now assemble the physical ingredients laid out in sections 4.1 and 4.2 into a sketch of how consumption and repulsion combine in an inviscid, wind-driven disc. Following by analogy our analysis in section 2.1 for a viscous disc, we first write down mass conservation (see equation 1 and Figure

1):

$$\begin{aligned} \dot{M}_+ &= \dot{M}_- + \dot{M}_p \\ 2\pi\Sigma_+r|c| &= 2\pi\Sigma_-r|c| + \dot{M}_p \\ &= 2\pi\Sigma_-r|c| + A\Sigma_p \end{aligned} \quad (49)$$

where in lieu of the viscosity we now have $r|c|$. After replacing Σ_- in (49) using our momentum relation (48), we have

$$\Sigma_+ \sim (1 + \tilde{B}_{\text{inv}})\Sigma_p + \frac{A}{2\pi r|c|}\Sigma_p \quad (50)$$

which implies the outer gap contrast

$$\frac{\Sigma_p}{\Sigma_+} \sim \frac{1}{1 + A/(2\pi r|c|) + \tilde{B}_{\text{inv}}} \quad (51)$$

As in the viscous case (equation 11), we see here that consumption ($A/(2\pi r|c|)$) and repulsion (\tilde{B}_{inv}) add. Taking A to be the Bondi value (equation 25) gives the ratio

$$\begin{aligned} \frac{A_{\text{Bondi}}/(2\pi r|c|)}{\tilde{B}_{\text{inv}}} &\sim \frac{0.5}{2\pi} \frac{h^{353/49}}{m^2(\Omega t)^{39/49}} \frac{\Omega r_p}{|c|} \\ &\sim 0.04 \left(\frac{M_p}{0.1 M_J}\right)^{-2} \left(\frac{t}{3 \text{ Myr}}\right)^{-39/49} \times \\ &\quad \left(\frac{|c|}{4 \text{ cm/s}}\right)^{-1} \left(\frac{r_p}{10 \text{ au}}\right)^{489/196} \end{aligned} \quad (52)$$

which informs us that repulsion dominates consumption ($\tilde{B}_{\text{inv}} > A_{\text{Bondi}}/(2\pi r|c|)$) when

$$\begin{aligned} M_p > M_{\text{repulsion,inv}} &\sim 0.02 M_J \left(\frac{t}{3 \text{ Myr}}\right)^{-39/98} \times \\ &\quad \left(\frac{|c|}{4 \text{ cm/s}}\right)^{-1/2} \left(\frac{r_p}{10 \text{ au}}\right)^{489/392} \end{aligned} \quad (53)$$

That repulsion dominates consumption even for small masses is in contrast to the viscous case (see equation 31 for $M_{\text{repulsion,visc}}$). Repulsion-dominated gaps are symmetric between the inner and outer discs (equations 48 and 51):

$$\begin{aligned} \Sigma_p/\Sigma_- &\sim \Sigma_p/\Sigma_+ \sim 1/(1 + \tilde{B}_{\text{inv}}) \\ &\sim 2 \times 10^{-3} \left(\frac{h}{0.054}\right)^{549/49} \left(\frac{10^{-4}}{m}\right)^4 \left(\frac{3 \text{ Myr}}{t}\right)^{39/49} \end{aligned} \quad (54)$$

where for the last equality we have assumed that the gaps are deep ($\tilde{B}_{\text{inv}} > 1$). Under these conditions, we may estimate a final accreted planet mass by time-integrating

$$\begin{aligned} \dot{M}_p &= A_{\text{Bondi}}\Sigma_p \\ &\sim A_{\text{Bondi}} \frac{\Sigma_+}{\tilde{B}_{\text{inv}}} \\ &\sim \frac{A_{\text{Bondi}}}{\tilde{B}_{\text{inv}}} \frac{M_{\text{disc}}}{2\pi(ct_{\text{adv}})^2} \frac{|c|t_{\text{adv}}}{r_p} e^{-r_p/(|c|t_{\text{adv}})} e^{-t/t_{\text{adv}}} \end{aligned} \quad (55)$$

from $t = 0$ to ∞ , where for Σ_+ we have employed the no-planet solution (46). This last approximation is analogous to the one we made in (37) for a viscous disc. Equation (55)

integrates to yield

$$\begin{aligned}
 M_{\text{final,inv}} &\sim \left[\frac{1.5}{2\pi} \Gamma\left(\frac{10}{49}\right) \left(\frac{M_{\text{disc}}}{M_{\star}}\right) \left(\frac{r_{\text{p}}}{|c|t_{\text{adv}}}\right) \right. \\
 &\quad \left. \times h^{353/49} (\Omega t_{\text{adv}})^{10/49} e^{-r_{\text{p}}/(|c|t_{\text{adv}})} \right]^{1/3} M_{\star} \\
 &\sim 0.3 M_{\text{J}} \left(\frac{M_{\text{disc}}}{15.5 M_{\text{J}}}\right)^{1/3} \left(\frac{r_{\text{p}}}{10 \text{ au}}\right)^{163/196} e^{-r_{\text{p}}/(3|c|t_{\text{adv}})} \\
 &\quad \text{(repulsion-limited)} \tag{56}
 \end{aligned}$$

where Γ is the gamma function, and the numerical evaluation uses our fiducial parameters including $|c| = 4$ cm/s, $t_{\text{adv}} = 3$ Myr, and $M_{\star} = 1M_{\odot}$. Our estimated final mass of $0.3 M_{\text{J}}$ at $r_{\text{p}} = 10$ au remains smaller than $M_{\text{thermal}} \simeq 0.5 M_{\text{J}}$ and so our use of A_{Bondi} is self-consistent.

Our expression (56) for $M_{\text{final,inv}}$ resembles equation (19) of [Ginzburg & Chiang \(2019a\)](#); ours is an improvement as we have accounted explicitly for the transport properties of the disc through the radial velocity c (see the discussion of transport-limited accretion in their section 4.1).

4.4 Numerical simulations

We test the ideas in section 4.3 by numerically solving the continuity equation (45) and the momentum equation (48). To model the planetary mass sink in equation (45), we utilize the same sub-grid procedure of section 2.2, replacing equation (24) with

$$\dot{M}_{\text{p}}(t) = A \times \frac{\Sigma(r_{\text{p}}, t)}{1 + \tilde{B}_{\text{inv}}} \tag{simulation} \tag{57}$$

where $\Sigma(r_{\text{p}}, t)$ is the grid-level surface density in the bin containing the planet, and A and \tilde{B}_{inv} are given by equations (25)–(26) and (47), respectively. The initial mass of the planet is set to $M_{\text{p}}(0) = 0.1 M_{\text{J}}$ (we will see that using smaller initial masses hardly changes the outcome). We solve the advective portion of equation (45) with a first-order upwind scheme (e.g., [Press et al. 2007](#)) applied to a grid that extends from $r_{\text{in}} = 0.01$ au to $r_{\text{out}} = 500$ au across 300 cells uniformly spaced in $\log r$. We fix $c = -4$ cm/s and initialize the grid using (46), with $t_{\text{adv}} = 3$ Myr and $M_{\text{disc}} = 15.5 M_{\text{J}} = 0.015 M_{\odot}$, the same value chosen for our viscous disc calculations. Our timestep is set to $\Delta t = 0.2 \Delta r_{\text{min}}/|c|$, where $\Delta r_{\text{min}} = 3 \times 10^{-3}$ au is our smallest bin width. Other disc properties such as $h(r)$ and $\Omega(r)$ are the same as before. For the outer boundary condition we impose a ghost cell just outside r_{out} where the surface density is fixed at 0.

Figure 6 (the inviscid counterpart to Figure 2) shows $\Sigma(r)$ at $t = t_{\text{adv}}$ when M_{p} has grown to $0.3 M_{\text{J}}$, illustrating many of the features anticipated from our analytic treatment. Without a planet, the surface density profile follows $r^{-1} \exp[-r/(|c|t_{\text{adv}})]$ as expected from equation (46). With a planet, a gap is created that is nearly symmetric between the inner and outer discs, and whose depth is dominated by Lindblad repulsion (enforced by our sub-grid scheme), not consumption (equation 54). The inviscid gap is deep (scaling as m^{-4} ; [Ginzburg & Sari 2018](#); [Ginzburg & Chiang 2019a](#); see also [Duffell 2020](#)). Figure 7 (analogous to Figure 4) provides snapshots of $\Sigma(r)$ and $\dot{M}_{\text{disc}}(r)$ taken at different times, and Figure 8 (analogous to Figure 5) plots $M_{\text{p}}(t)$. Unlike in a viscous disc, our example planet in an inviscid disc does not consume most of the disc mass exterior to its

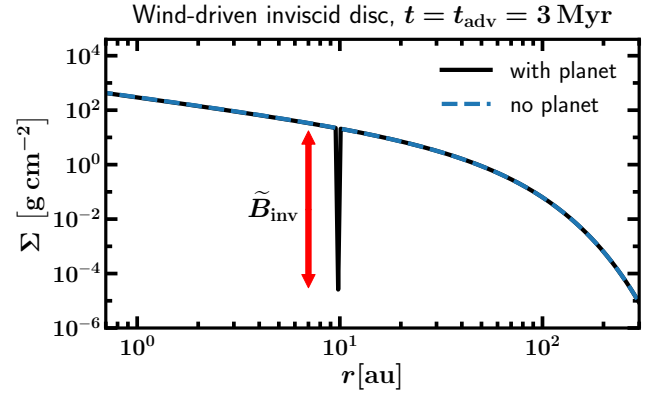


Figure 6. How the surface density profile of an inviscid disc responds to a planet that consumes disc gas and repels gas away by Lindblad torques. The planet, located at $r_{\text{p}} = 10$ au, freely accretes starting from a seed mass of $0.1 M_{\text{J}}$; the Σ profile shown here is taken at a time $t = t_{\text{adv}} = 3$ Myr, when the planet has grown to $\sim 0.3 M_{\text{J}}$ (see also Figure 8). As is the case throughout this paper, the planet’s gap is not spatially resolved, but is modeled as a single cell. The “true” surface density inside this cell equals the grid-level Σ lowered by a factor of \tilde{B}_{inv} , whose magnitude is given by the red double-tipped arrow. The gap is repulsion and not consumption dominated ($\tilde{B}_{\text{inv}} > A/(2\pi r|c|)$, equation 52); as such, the gap is symmetric in the sense that the surface density contrast with the outer disc is practically the same as with the inner disc. This figure is the inviscid counterpart to Figure 2 which was made for a viscous disc.

orbit; the disc accretion rate profile $\dot{M}_{\text{disc}}(r)$ is not much affected by the planet except during an initial transient phase at $t < t_{\text{adv}}$. We see a need for a high radial accretion velocity $|u_r|$ within the gap (see also section 3.1): to ensure that \dot{M}_{disc} grades smoothly across the gap as shown in Figure 7, $|u_r|$ must increase in proportion to the gap contrast Σ/Σ_{p} . Inviscid gap contrasts are on the order of 10^5 , and so $|u_r| \sim 10^5 |c| \sim 4$ km/s, comparable to the orbital velocity. Note that simulations of planets in inviscid discs have not reproduced the deep gaps expected from our analytics, finding gap contrasts only up to a factor of ~ 10 (e.g., [Fung & Chiang 2017](#); [McNally et al. 2019, 2020](#)). On the one hand the simulations are of limited duration and so their gaps may not have fully developed; on the other hand, the simulations allow for orbital migration and hydrodynamical instabilities, effects which may prevent gaps from becoming too deep in reality.

That the disc accretion flow proceeds largely unimpeded from outside to inside the planet’s orbit is a consequence of the gap being repulsion-dominated (equation 15, with v replaced by $r|c|$). The planet diverts such a small fraction of the disc flow that it grows from $0.1 M_{\text{J}}$ to only $0.3 M_{\text{J}}$; most of the original $15.5 M_{\text{J}}$ contained in the disc drains onto the star. Figure 8 also shows that reducing the initial seed mass to $M_{\text{p}}(0) = 0.01 M_{\text{J}}$ hardly affect the final mass.

5 SUMMARY AND DISCUSSION

Planets open gaps in circumstellar discs in two ways: by repelling material away via Lindblad torques, and by consuming local disc gas. Measured relative to the disc outside the

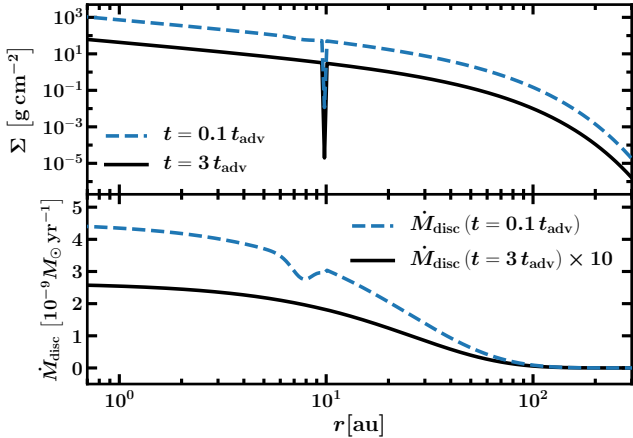


Figure 7. Snapshots of the surface density profile $\Sigma(r)$ and disc accretion rate $\dot{M}_{\text{disc}}(r) = -2\pi\Sigma u_r r$ (> 0 for accretion toward the star) for a planet embedded in an inviscid, wind-driven disc. The planet mass is allowed to freely grow starting from $M_p(0) = 0.1 M_J$; the masses corresponding to the plotted times are $0.27 M_J$ ($t = 0.1 t_{\text{adv}} = 0.3$ Myr) and $0.34 M_J$ ($t = 3 t_{\text{adv}} = 9$ Myr; see also Figure 8). At $t = 3 t_{\text{adv}}$, the disc has relaxed into a quasi-steady state in the presence of the planetary mass sink, and $\dot{M}_{\text{disc}}(r)$ looks essentially the same as it would without the planet; the accretion rate onto the planet is negligible compared to the disc accretion rate—the gap is repulsion-dominated—and so the disc is not materially affected. Even at $t = 0.1 t_{\text{adv}}$, the interior surface density Σ_{in} and \dot{M}_{disc} depress by only $\sim 15\%$ because of consumption.

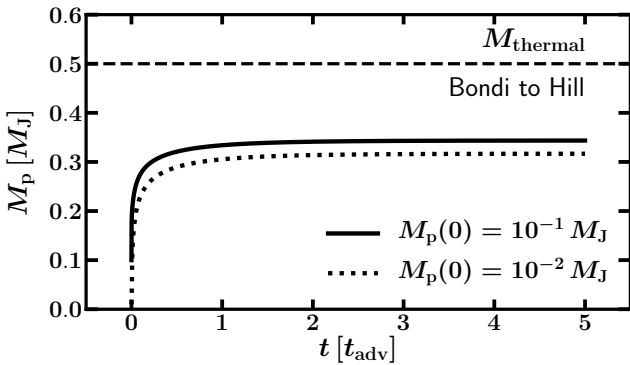


Figure 8. Mass evolution of a planet embedded at $r_p = 10$ au in an inviscid but still accreting disc of initial mass $M_{\text{disc}} = 15.5 M_J$. Within ~ 1 disc advection time t_{adv} , the planet, whose gap is repulsion-dominated ($\tilde{B}_{\text{inv}} > A_{\text{Bondi}}/(2\pi r_p |c|)$), grows to a mass of $\sim 0.35 M_J$. The final planet mass varies by only $\sim 10\%$ when the initial seed mass $M_p(0)$ varies by a factor of 10. This figure is the inviscid counterpart to Figure 5 which was made for a viscous disc.

planet’s orbit, the two effects are additive: both repulsion and consumption add to deepen the planet’s gap relative to the outer disc (see equation 11 or 51). Relative to the inner disc, downstream of the mass sink presented by the planet, the gap surface density contrast is set by repulsion only (see equation 10 or 48).

Many planet formation studies (e.g., Tanigawa &

Tanaka 2016; Lee 2019) take the planet’s hydrodynamically-limited accretion rate $\dot{M}_p = \min(\dot{M}_{\text{hydro}}, \dot{M}_{\text{disc}})$, where \dot{M}_{hydro} is the planetary accretion rate computed according to the hydrodynamics of flows in the immediate vicinity of the planet, and \dot{M}_{disc} is the local disc accretion rate (the mass crossing the planet’s orbital radius, per time). Prescribing the planet’s accretion rate in this way is equivalent to comparing consumption, as measured by the “consumption coefficient” $A \equiv \dot{M}_p/\Sigma_p$, where Σ_p is the surface density inside the gap, and repulsion, as measured by the “repulsion coefficient” $B \equiv T/(\Sigma_p \Omega r^2)$, where T is the repulsive planetary torque and Ωr^2 is the angular momentum per unit mass (see also Tanigawa & Tanaka 2016 and Tanaka et al. 2020 who use the same framework). Under consumption-limited conditions ($A/(3\pi) > B$), the planet’s accretion rate saturates to nearly the disc’s accretion rate: $\dot{M}_p = \min(\dot{M}_{\text{hydro}}, \dot{M}_{\text{disc}}) = \dot{M}_{\text{disc}}$. Otherwise, under repulsion-limited conditions ($A/(3\pi) < B$), $\dot{M}_p = \min(\dot{M}_{\text{hydro}}, \dot{M}_{\text{disc}}) = \dot{M}_{\text{hydro}}$.

5.1 Final planet masses

In conventional viscous discs with large enough α -diffusivities² and our assumed parameters, planets begin their growth under consumption-dominated conditions and possibly continue their growth under repulsion-dominated conditions, arriving at final masses well in excess of a Jupiter. We show in Figure 9 the final mass of a planet embedded in an $\alpha = 10^{-3}$ disc, as a function of the planet’s orbital distance r_p , computed using our numerical code of sections 2–3. Final planet masses increase gradually from $4 M_J$ at 1 au, to $8 M_J$ at 30 au, in a disc of initial mass $M_{\text{disc}} = 15.5 M_J = 0.015 M_\odot$. In a disc $5\times$ more massive, the corresponding range of planet masses is $9\text{--}20 M_J$. The final masses are not sensitive to α insofar as α controls only the timescale over which the disc evolves (modulo disc dispersal by some other means, e.g., photoevaporation; see Tanaka et al. 2020). Final masses do depend on the initial mass of the disc, scaling as $M_{\text{disc}}^{3/7}$ under repulsion-dominated conditions (equation 39) and M_{disc}^1 under consumption-dominated conditions (equation 42 or 43). The trend of final planet mass with distance shown in Figure 9 follows, for the most part, the trend predicted for repulsion-limited conditions, except at large r_p where consumption dominates. The final mass profiles in Figure 9 recall those of the super-Jupiters in the HR 8799 system; the four planets, located between 15 and 70 AU of their host star, have practically the same mass, about $6\text{--}7 M_J$ (Wang et al. 2018).

Initially and everywhere in a viscous disc, a planet, despite opening a gap, consumes practically all of the disc gas that tries to diffuse past its orbit (equation 14 with $A/(3\pi) > B > \nu$, where ν is the disc viscosity). This consumption-limited behaviour persists up to a repulsion mass $M_{\text{repulsion,visc}} \approx 5 M_J [r_p/(10 \text{ au})]^{9/16}$ (equation 31), above which repulsion dominates. The repulsion mass is not the thermal mass M_{thermal} (equation 28), but exceeds it by a factor of $\sim h^{-3/4}$, where h is the disc aspect ratio. Growth continues more slowly at $M_p > M_{\text{repulsion,visc}}$, with the planet

² If the Shakura-Sunyaev $\alpha \lesssim 10^{-4}$, discs respond to planetary torques as if they were inviscid (Ginzburg & Chiang 2019a, their fig. 1).

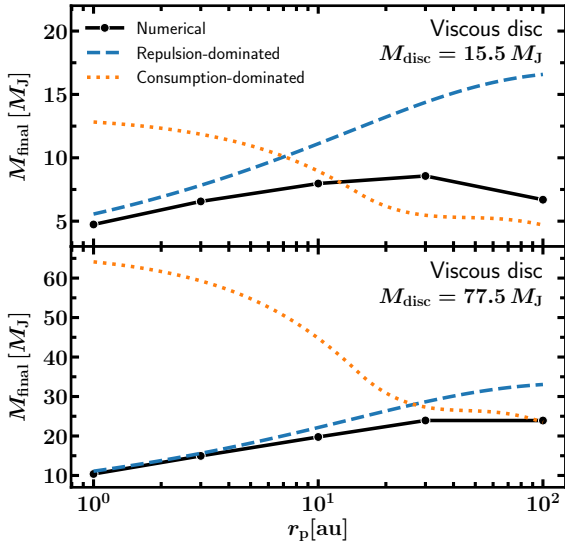


Figure 9. Final planet masses grown from viscous discs having $\alpha = 10^{-3}$ and varying total mass (top vs. bottom panels). Planet masses are initialized at $0.1 M_J$ and grown using the 1D numerical code of section 3, which utilizes the repulsive gap contrast of Kanagawa et al. (2015; see also Duffell & MacFadyen 2013 and Fung et al. 2014) and gas accretion that switches from Bondi to Hill at the thermal mass. Points are plotted at $t = 50 t_1 = 85$ Myr, where $t_1 = r_1^2 / [3\nu(r_1)]$ is the viscous diffusion time at $r_1 = 30$ au. Analytic curves are given by equation (38) for the repulsion limit (dashed blue), and equations (42)–(43) for the consumption limit (dotted orange), also evaluated at $t = 50 t_1$. At most orbital distances, planet mass growth is limited by repulsion-dominated gaps; only at the largest distances, where the disc aspect ratio is large, are gaps relatively harder to open and conditions remain consumption-limited. The analytics, which are derived assuming the planet mass is small compared to the disc mass, are a better guide for the more massive disc in the bottom panel.

mass increasing beyond $M_{\text{repulsion,visc}}$ by up to a factor of ~ 4 for our parameter choices.

Equation (38) gives an approximate analytic expression for the planet mass vs. time during this final repulsion-limited stage. It predicts that planet masses are of order $10 M_J$ by the time the disc dissipates. This result is derived by assuming the planet accretes at a rate that scales as $A_{\text{Hill}} = 2.2 \Omega r^2 m^{2/3}$, where m is the planet-to-star mass ratio; this prescription is commonly adopted by hydrodynamical simulations of planet-disc interactions, and might be appropriate for super-thermal masses. If instead of A_{Hill} we use the empirical formula $A_{\text{TW}} = 0.29 \Omega r^2 m^{4/3} / h^2$ drawn from 2D numerical simulations by Tanigawa & Watanabe (2002), then the mass above which repulsion dominates changes to $M_{\text{repulsion,visc,TW}} \approx 9 M_J [r/(10 \text{ au})]^{3/8}$, nearly twice the value of $M_{\text{repulsion,visc}}$ derived using the Hill scaling. Using A_{TW} leads to a more extended consumption-dominated growth phase, and final planet masses larger by order-unity factors compared to those of the solid curves in Figure 9. Overall, it appears that in viscous discs, planets accrete a not-small fraction of the disc mass, which can be many tens of Jupiter

masses (Tripathi et al. 2017, their fig. 10; see also Powell et al. 2019). This is in agreement with Tanaka et al. (2020), who limit giant planet growth by incorporating photoevaporative mass loss from the disc.

In inviscid discs, conditions tend to be repulsion-dominated even at low planet masses. Without viscosity or turbulent transport to compete against, planetary Lindblad torques carve deep gaps that are repulsion-dominated even for sub-thermal planets accreting at the Bondi rate (equation 52). Repulsion-dominated gaps are symmetric in the sense that gap contrasts between the outer and inner discs are the same; accordingly, disc accretion rates are nearly continuous across the gap (e.g., Figure 7), which means that most of the disc mass is not diverted onto the planet (in the language of Tanigawa & Tanaka 2016, $\dot{M}_p = \min(\dot{M}_{\text{hydro}}, \dot{M}_{\text{disc}}) = \dot{M}_{\text{hydro}}$). Maintaining the disc accretion rate across a gap demands that the radial accretion velocity within the gap be as large as the gap is deep. Whether such fast inflows are possible, and whether inviscid gaps can be as deep as expected from our analytics (cf. numerical simulations that find only shallow gaps; Fung & Chiang 2017; McNally et al. 2019, 2020), are unresolved issues.

Figure 10, analogous to Figure 9, shows that final planet masses in our model inviscid discs range between ~ 0.05 and $1 M_J$, more than an order-of-magnitude smaller than their viscous disc counterparts. For the most part, the masses computed for inviscid discs using our numerical 1D code are well reproduced by equation (56), derived in the repulsion limit. This formula, which predicts that final planet masses scale as $M_{\text{disc}}^{1/3}$ and $r_p^{163/196} \approx r_p^{0.83}$, is similar to that derived by Ginzburg & Chiang (2019a, their equation 19),³ and improves upon it by accounting for the structure and transport properties of the parent disc—specifically how the disc may accrete by shedding angular momentum through a magnetized surface wind (e.g., Bai 2016).

Orbital migration in viscous discs has been shown in numerical simulations to enhance \dot{M}_p relative to the migration-free case (e.g., Dürmann & Kley 2017). Including migration would only amplify our finding that final planet masses in viscous discs are large, approaching if not well within the regime of brown dwarfs. Accretion rates should also increase for planets migrating in inviscid, wind-driven discs; in 3D, strongly sub-thermal planets have been shown to migrate inward (McNally et al. 2020). We may need such enhancements in \dot{M}_p to explain, within an inviscid scenario, giant planets like our own Jupiter, i.e., to bring planet masses up to $1 M_J$ at distances of 1–10 au (Figure 10). On the other hand, sub-Jupiter masses, down to $\sim 0.1 M_J$ in many cases, are inferred from ALMA observations of disc gaps (Zhang et al. 2018), and suggest that planets there are strongly repelling inviscid gas.

The asymmetric gap we computed for the viscous disc model in Figure 2 suggests a strong, mostly one-sided migration torque forcing the planet inward. However, this is misleading because our numerical procedure does not spatially resolve the gap, whose true radial width lies between H (the pressure scale height) and r_p (Ginzburg & Sari 2018). Most of the migration torque is exerted by disc gas on the

³ Our final planet masses are a factor of ~ 3 lower than theirs, a consequence largely of their choice for h which is 50% larger.

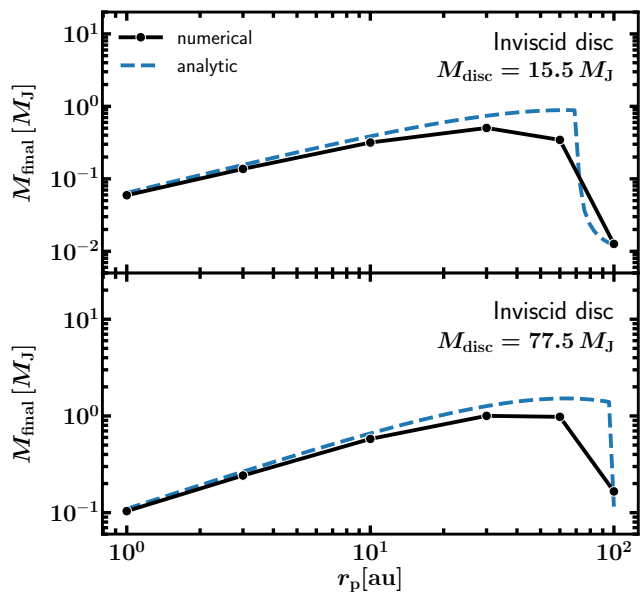


Figure 10. Final planet masses in an inviscid, wind-driven disc of varying mass (top vs. bottom panels). Planet masses are initialized at $0.01M_J$ and grown using the 1D numerical code of section 4.4, which uses the time-dependent gap contrast of Ginzburg & Chiang (2019a) to model repulsion, in a purely advective disc whose height-averaged radial accretion velocity is $c = -4$ cm/s and exponential drain-out time is $t_{\text{adv}} = 3$ Myr. Points are plotted after $5t_{\text{adv}} = 15$ Myr. They mostly respect equation (56), which gives final planet masses grown in repulsion-limited and deep ($\tilde{B}_{\text{inv}} > 1$) gaps (dashed curve not including the drop-off at the largest distances). At $r_p \sim 100$ au, the disc has such low density that the planet’s initial growth timescale M_p/\dot{M}_p is comparable to t_{adv} ; here there are not many doublings before the disc drains away. In this regime the planet does not open a substantial gap ($\tilde{B}_{\text{inv}} < 1$) and its final mass can be estimated analytically by integrating $\dot{M}_p = A_{\text{Bondi}}\Sigma$ with Σ given by the no-planet solution (46); the dashed curve is the minimum of the resulting expression (not shown) and (56).

bottoms of gaps, displaced radially from the planet by $\sim \pm H$, and here the actual surface density gradients, and of course the surface density itself, are small (see also Kanagawa et al. 2018).

5.2 Transitional discs

We have shown how a planet accreting from its parent disc can change the disc’s entire complexion. This make-over is most evident for a planet that siphons away most of the disc’s accretion flow—as it can in a viscously diffusing disc—carving out a consumption-limited gap that divides a gas-rich outer disc with surface density Σ_+ from a gas-poor inner one with surface density Σ_- . Transitional discs have just such an outer/inner structure (e.g., Espaillat et al. 2014; Dong et al. 2017), suggesting that they represent viscous discs whose inner regions are cleared by accreting planets (with dust filtration at the outer gap edge, and grain growth in the inner disc, enhancing the surface density contrast in dust over gas; Dong et al. 2012; Zhu et al. 2012).

In a viscous disc, a single accreting planet suffices to deplete the entire disc interior to its orbit. The 2D single-

planet simulations of Zhu et al. (2011) bear this out; they find an outer vs. inner disc contrast of $\Sigma_+/\Sigma_- \sim 10$ for a $1M_J$ planet that accretes at the Hill rate from a disc of $h \approx 0.05$ (their fig. 1, model P1A1). This numerical result agrees with our analytic theory, which predicts according to equations (15) and (30) that

$$\frac{\Sigma_+}{\Sigma_-} \approx \frac{A_{\text{Hill}}}{3\pi B} \approx 7 \left(\frac{M_p}{M_J} \right)^{-4/3} \left(\frac{h}{0.05} \right)^3 \quad (58)$$

for a consumption-dominated and deep gap with $A_{\text{Hill}}/(3\pi) > B > \nu$, where ν is the disc viscosity. In steady state, $\Sigma_+/\Sigma_- = \dot{M}_+/\dot{M}_-$, the ratio of outer-to-inner disc accretion rates. A value of $\dot{M}_+/\dot{M}_- \sim 10$, as we have found for the above parameters, accords with the observation that the median accretion rate for stars hosting transitional discs is lower than that of stars hosting non-transitional discs by a factor of ~ 10 (Najita et al. 2007; Kim et al. 2013). However, the corresponding factor-of-10 reduction in Σ seems too small to match observed gas depletions in transitional disc cavities. In the disc studied in CO by Dong et al. (2017), the gas surface density declines by $\sim 10^3$ from $r = 70$ au to 15 au. As recognized by Zhu et al. (2011; see also Owen 2016), it is a challenge to simultaneously explain how disc inner cavities can be strongly depleted in density while their central stars continue to accrete at near-normal rates.

This challenge seems more easily met in the repulsion limit, where deep gaps are carved by planets which alter the disc accretion flow only modestly—assuming radial accretion velocities within the gap are large enough to maintain mass transport rates across it.

The repulsion limit is attained in viscous discs by planets having $M > M_{\text{repulsion,visc}} \approx 5.3 M_J [r/(10 \text{ au})]^{9/16}$, or in inviscid discs by planets having $M > M_{\text{repulsion,inv}} \approx 0.02 M_J [r/(10 \text{ au})]^{489/392}$. In both cases, multiple planets with adjoining gaps would be required to evacuate transition disc cavities spanning decades in radius—more planets in a viscous scenario where each gap has a radial width closer to H , and fewer in an inviscid scenario where each gap is of order $r_p > H$ wide (Ginzburg & Sari 2018; note that widths are not captured by our single-grid-point treatment of gaps). The inviscid picture requires only super-Earth masses and appeals more, insofar as observations seem to have already ruled out transitional discs containing families of super-Jupiters as required in the viscous scenario. Inviscid discs can still accrete, either by virtue of magnetized winds (Bai 2016; Wang & Goodman 2017), or by the repulsive torques of their embedded planets (Goodman & Rafikov 2001; Sari & Goldreich 2004; Fung & Chiang 2017).

ACKNOWLEDGEMENTS

We thank Xuening Bai, Jeffrey Fung, Willy Kley, Eve Lee, James Owen, and Hidekazu Tanaka for helpful exchanges. An anonymous referee provided an encouraging report. EC acknowledges NASA grants 80NSSC19K0506 and NNX15AD95G/NEXSS. SG is supported by the Heising-Simons Foundation through a 51 Pegasi b Fellowship. MMR and RMC acknowledge support from NSF CAREER grant number AST-1555385.

DATA AVAILABILITY

The code underlying this article will be shared on reasonable request to the corresponding author.

REFERENCES

Bai X.-N., 2011, *ApJ*, **739**, 50
 Bai X.-N., 2016, *ApJ*, **821**, 80
 Bai X.-N., Stone J. M., 2013, *ApJ*, **769**, 76
 Bai X.-N., Ye J., Goodman J., Yuan F., 2016, *ApJ*, **818**, 152
 Blandford R. D., Payne D. G., 1982, *MNRAS*, **199**, 883
 D’Angelo G., Kley W., Henning T., 2003, *ApJ*, **586**, 540
 Dong R., et al., 2012, *ApJ*, **750**, 161
 Dong R., et al., 2017, *ApJ*, **836**, 201
 Duffell P. C., 2015, *ApJ*, **807**, L11
 Duffell P. C., 2020, *ApJ*, **889**, 16
 Duffell P. C., Chiang E., 2015, *ApJ*, **812**, 94
 Duffell P. C., MacFadyen A. I., 2013, *ApJ*, **769**, 41
 Duffell P. C., Haiman Z., MacFadyen A. I., D’Orazio D. J., Farris B. D., 2014, *ApJ*, **792**, L10
 Dürmann C., Kley W., 2015, *A&A*, **574**, A52
 Dürmann C., Kley W., 2017, *A&A*, **598**, A80
 Espaillat C., et al., 2014, in Beuther H., Klessen R. S., Dullemond C. P., Henning T., eds, *Protostars and Planets VI*. p. 497 ([arXiv:1402.7103](https://arxiv.org/abs/1402.7103)), doi:10.2458/azu_uapress_9780816531240-ch022
 Flaherty K. M., et al., 2017, *ApJ*, **843**, 150
 Frank J., King A., Raine D. J., 2002, *Accretion Power in Astrophysics: Third Edition*
 Fung J., Chiang E., 2016, *ApJ*, **832**, 105
 Fung J., Chiang E., 2017, *ApJ*, **839**, 100
 Fung J., Shi J.-M., Chiang E., 2014, *ApJ*, **782**, 88
 Fung J., Zhu Z., Chiang E., 2019, *ApJ*, **887**, 152
 Gammie C. F., 1996, *ApJ*, **457**, 355
 Ginzburg S., Chiang E., 2019a, *MNRAS*, **487**, 681
 Ginzburg S., Chiang E., 2019b, *MNRAS*, **490**, 4334
 Ginzburg S., Sari R., 2018, *MNRAS*, **479**, 1986
 Goldreich P., Sari R., 2003, *ApJ*, **585**, 1024
 Goldreich P., Tremaine S., 1980, *ApJ*, **241**, 425
 Goldreich P., Tremaine S., 1982, *ARA&A*, **20**, 249
 Goodman J., Rafikov R. R., 2001, *ApJ*, **552**, 793
 Hartmann L., Calvet N., Gullbring E., D’Alessio P., 1998, *ApJ*, **495**, 385
 Kanagawa K. D., Muto T., Tanaka H., Tanigawa T., Takeuchi T., Tsukagoshi T., Momose M., 2015, *ApJ*, **806**, L15
 Kanagawa K. D., Tanaka H., Szuszkiewicz E., 2018, *ApJ*, **861**, 140
 Kim K. H., et al., 2013, *ApJ*, **769**, 149
 Kimmig C. N., Dullemond C. P., Kley W., 2020, *A&A*, **633**, A4
 Kley W., Dirksen G., 2006, *A&A*, **447**, 369
 Kley W., Nelson R. P., 2012, *ARA&A*, **50**, 211
 Lee E. J., 2019, *ApJ*, **878**, 36
 Lin D. N. C., Papaloizou J., 1986, *ApJ*, **309**, 846
 Lubow S. H., D’Angelo G., 2006, *ApJ*, **641**, 526
 Lynden-Bell D., Pringle J. E., 1974, *MNRAS*, **168**, 603
 McNally C. P., Nelson R. P., Paardekooper S.-J., Benítez-Llambay P., 2019, *MNRAS*, **484**, 728
 McNally C. P., Nelson R. P., Paardekooper S.-J., Benítez-Llambay P., Gressel O., 2020, *MNRAS*, **493**, 4382
 Morbidelli A., Szulágyi J., Crida A., Lega E., Bitsch B., Tanigawa T., Kanagawa K., 2014, *Icarus*, **232**, 266
 Muley D., Fung J., van der Marel N., 2019, *ApJ*, **879**, L2
 Najita J. R., Strom S. E., Muzerolle J., 2007, *MNRAS*, **378**, 369
 Owen J. E., 2016, *Publ. Astron. Soc. Australia*, **33**, e005
 Papaloizou J. C. B., Nelson R. P., Masset F., 2001, *A&A*, **366**, 263

Perez-Becker D., Chiang E., 2011, *ApJ*, **727**, 2
 Pinte C., Dent W. R. F., Ménard F., Hales A., Hill T., Cortes P., de Gregorio-Monsalvo I., 2016, *ApJ*, **816**, 25
 Powell D., Murray-Clay R., Pérez L. M., Schlichting H. E., Rosenthal M., 2019, *ApJ*, **878**, 116
 Press W. H., Teukolsky S. A., Vetterling W. T., Flannery B. P., 2007, *Numerical Recipes 3rd Edition: The Art of Scientific Computing*, 3 edn. Cambridge University Press, New York, NY, USA
 Sari R., Goldreich P., 2004, *ApJ*, **606**, L77
 Shakura N. I., Sunyaev R. A., 1973, *A&A*, **24**, 337
 Szulágyi J., Morbidelli A., Crida A., Masset F., 2014, *ApJ*, **782**, 65
 Tanaka H., Murase K., Tanigawa T., 2020, *ApJ*, **891**, 143
 Tanigawa T., Tanaka H., 2016, *ApJ*, **823**, 48
 Tanigawa T., Watanabe S.-i., 2002, *ApJ*, **580**, 506
 Tripathi A., Andrews S. M., Birnstiel T., Wilner D. J., 2017, *ApJ*, **845**, 44
 Wang L., Goodman J. J., 2017, *ApJ*, **835**, 59
 Wang J. J., et al., 2018, *AJ*, **156**, 192
 Zhang S., et al., 2018, *ApJ*, **869**, L47
 Zhu Z., Nelson R. P., Hartmann L., Espaillat C., Calvet N., 2011, *ApJ*, **729**, 47
 Zhu Z., Nelson R. P., Dong R., Espaillat C., Hartmann L., 2012, *ApJ*, **755**, 6

APPENDIX A: ANALYTIC STEADY-STATE SOLUTION FOR Σ AND \dot{M} FOR VISCOUS DISC WITH PLANET

In this appendix we provide an analytic expression for the surface density profile of a disc with an embedded planet. Our derivation here is more careful than our order-of-magnitude sketch in section 2.1, and similar to that presented in Lubow & D’Angelo (2006, their section 2.4), with a couple of differences: we reduce the surface density at the planet’s location by a factor $1 + B/\nu$ to account for repulsive Lindblad torques (see section 2.1), and we express our solution in terms of the surface density at infinity as opposed to the surface density at the planet’s location.

Using the same notation as in section 2.1, and neglecting for the moment the Lindblad torque, the equations of mass and angular momentum conservation with a mass sink at $r = r_p$ read

$$\frac{1}{r} \frac{d(\mu u_r r / \nu)}{dr} = -\frac{\dot{M}_p}{2\pi r} \delta(r - r_p) \quad (\text{A1})$$

$$\frac{r^2 \Omega \mu u_r}{\nu} = -\frac{d}{dr} (3\mu \Omega r^2) \quad (\text{A2})$$

where u_r is the radial velocity and $\mu \equiv \Sigma \nu$. Equation (A1) indicates that the mass flow rate $\dot{M}_+ = -2\pi \mu_+ u_r r / \nu$ is spatially constant in regions exterior to the planet’s orbit (the outer disc), and likewise for \dot{M}_- in regions interior to the planet’s orbit (the inner disc):

$$\dot{M}_- = \dot{M}_+ - A \frac{\mu_p}{\nu_p} \quad (\text{A3})$$

where we have used $\dot{M}_p = A \mu_p / \nu_p$ and $\nu_p \equiv \nu(r_p)$. Since \dot{M}_- and \dot{M}_+ are constants, equation (A2) can be solved to yield

$$3\pi \mu_{\pm}(r) = \dot{M}_{\pm} + \frac{C_{\pm}}{\sqrt{r}} \quad (\text{A4})$$

where C_{\pm} are integration constants. For the inner disc we use the boundary condition $\mu_{-}(r_{\star}) = 0$, whence

$$3\pi\mu_{-}(r) = \dot{M}_{-} \left(1 - \sqrt{\frac{r_{\star}}{r}} \right). \quad (\text{A5})$$

Following our treatment in the main text, we encode the planetary gap caused by Lindblad torques at a sub-grid level, i.e., we force the surface density at the planet's location to be depleted relative to the surface density just interior to the planet according to

$$\mu_p = \mu_{-}(r_p) (1 + B/\nu_p)^{-1} \quad (\text{A6})$$

where subscript p denotes the planet's location. For the outer disc, we fix the surface density at infinity, $\mu(\infty) = \mu_{\infty}$, so that

$$\dot{M}_{+} = 3\pi\mu_{\infty}. \quad (\text{A7})$$

Then from equations (A3), (A5), and (A6) we have

$$\frac{\mu_p}{\mu_{\infty}} = \frac{1}{\frac{1}{1-\sqrt{r_{\star}/r_p}} + \left(\frac{A}{3\pi} + \frac{B}{1-\sqrt{r_{\star}/r_p}} \right) / \nu_p} \quad (\text{A8})$$

which can be compared to equation (11). We may also solve for

$$\frac{\dot{M}_p}{\dot{M}_{+}} = \frac{A/(3\pi\nu_p)}{\frac{1}{1-\sqrt{r_{\star}/r_p}} + \left(\frac{A}{3\pi} + \frac{B}{1-\sqrt{r_{\star}/r_p}} \right) / \nu_p} \quad (\text{A9})$$

$$\frac{\dot{M}_{-}}{\dot{M}_{+}} = \frac{1 + B/\nu_p}{1 + \left[\frac{A}{3\pi} \left(1 - \sqrt{\frac{r_{\star}}{r_p}} \right) + B \right] / \nu_p} \quad (\text{A10})$$

which can be compared to equations (14) and (15). Finally, stitching the outer disc solution to the inner disc solution implies $\mu_{+}(r_p) = \mu_{-}(r_p) = \mu_p(1 + B/\nu_p)$ and

$$3\pi\mu_{+}(r) = 3\pi\mu_{\infty} \left[1 - \sqrt{\frac{r_p}{r}} \left(1 - \frac{\mu_p(1 + B/\nu_p)}{\mu_{\infty}} \right) \right]. \quad (\text{A11})$$

The equations above mirror the results in section 2.1, with the addition of a factor of 3π (see section 2.2) and the factor of $1 - \sqrt{r_{\star}/r_p}$ which accounts for the star's ability to divert material from the planet.

In Figure A1 we plot equations (A5), (A6) and (A11), adopting parameters as close as possible to those used in the top panel of Figure 2 so that we may compare the numerical result there to the analytic result here (see caption to Figure A1 for details).

APPENDIX B: MAGNETIZED WINDS AND DISC ACCRETION

We motivate here our simple, constant accretion velocity model for a wind-driven disc using the numerical simulations of Bai and collaborators. From continuity (equations 1, 6, and 9 of Bai 2016),

$$\begin{aligned} \frac{\partial \Sigma}{\partial t} &= + \frac{1}{2\pi r} \frac{\partial \dot{M}_{\text{disc}}}{\partial r} - \frac{1}{2\pi r} \frac{\partial \dot{M}_{\text{wind}}}{\partial r} \\ &= + \frac{1}{2\pi r} \frac{\partial}{\partial r} \left[2(\lambda - 1)r \frac{\partial \dot{M}_{\text{wind}}}{\partial r} \right] - \frac{1}{2\pi r} \frac{\partial \dot{M}_{\text{wind}}}{\partial r} \end{aligned} \quad (\text{B1})$$

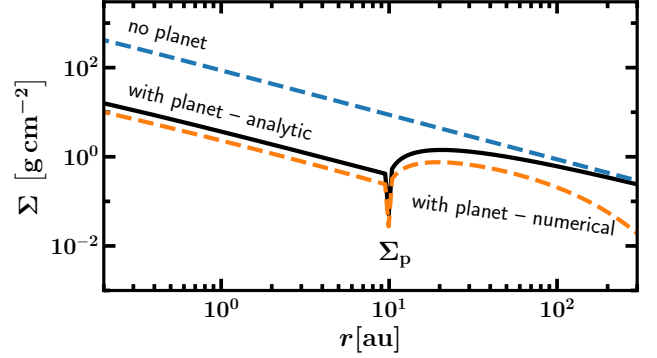


Figure A1. Analytic solution (black solid curve) for the surface density profile of a viscous disc perturbed by a planet, as given by equations (A5), (A6) and (A11), using parameters as close as possible to those used in the top panel of Figure 2, whose numerical result is overlaid here for comparison (orange dashed curve). For our unperturbed “no planet” disc (blue dashed curve) we use a power law of slope -1 and normalization at 1 au equal to the corresponding “no planet” curve in Figure 2. The A and B coefficients are taken from equations (25) and (27) for $M_p = 0.3 M_J$. The differences between the analytic and numeric curves mainly arise from the behaviour of the outermost disc near the turn-around “transition radius” (Lynden-Bell & Pringle 1974; Hartmann et al. 1998). This transition radius, which varies with time, does not appear in our steady-state solution.

where

$$\dot{M}_{\text{wind}}(r) = \int^r \frac{\partial \dot{M}_{\text{wind}}}{\partial r} dr \quad (\text{B2})$$

is the cumulative rate at which mass is carried to infinity by the wind (integrated over the disc within r). From equation (20) of Bai et al. (2016),

$$\frac{\partial \dot{M}_{\text{wind}}}{\partial r} = 2\pi r \rho_0 u_{p0} \quad (\text{B3})$$

where ρ_0 and u_{p0} are the volumetric mass density and poloidal velocity of the wind where it is launched, near the disc surface. All quantities subscripted with 0 are evaluated at the wind base (r_0, z_0) .

The disc accretion rate

$$\dot{M}_{\text{disc}} \equiv -2\pi \Sigma r u_r = 2(\lambda - 1)r \frac{\partial \dot{M}_{\text{wind}}}{\partial r} \quad (\text{B4})$$

for surface density Σ and radial velocity u_r is identical in definition to the variable \dot{M}_{disc} used throughout our paper. Unlike \dot{M}_{wind} , \dot{M}_{disc} is not a cumulative quantity, but measures the mass crossing a circle of radius r per unit time, and uses a sign convention such that $\dot{M}_{\text{disc}} > 0$ for $u_r < 0$.

Disc accretion by a wind hinges on the “magnetic lever arm”

$$\lambda = (r_A/r_0)^2 \quad (\text{B5})$$

where r_A is the Alfvén radius for the wind streamline running through r_0 . A lever arm $\lambda > 1$ enables $\dot{M}_{\text{disc}} > 0$ by having the wind carry away more specific angular momentum than the Keplerian disc has at r_0 . The fiducial wind model of Bai (2016, their fig. 2) has $(\lambda - 1)$ ranging from ~ 30 at $r = 0.3$ AU to ~ 2 at 30 AU; therefore the first term in (B1) dominates the second term by a factor of order $2(\lambda - 1) \sim 4-60$. Only the first term is modeled in our paper.

Bai (2016) and the magnetized disc wind literature dating back to Blandford & Payne (1982) parameterize the wind mass-loss rate in terms of the dimensionless mass loading parameter

$$\mu = \frac{\omega r_0}{B_{p0}} \times k = \frac{\omega r_0}{B_{p0}} \times \frac{4\pi\rho\mu_p}{B_p} \quad (\text{B6})$$

where k is the ratio of poloidal mass flux to poloidal field strength B_p (k is constant along a magnetic field line), and ω is the angular velocity of a field line, approximately equal to the Keplerian frequency Ω_K at r_0 . Note that μ (not to be confused with μ in Appendix A) varies with r from field line to field line. Evaluating μ at the wind base, we rewrite (B3) as

$$\frac{\partial \dot{M}_{\text{wind}}}{\partial r} = \frac{\mu B_{p0}^2}{2\omega} \quad (\text{B7})$$

(Bai et al. 2016, equation 21). Now parameterize B_{p0} in terms of the midplane plasma beta:

$$\beta_0 = \frac{8\pi}{B_{p0}^2} \frac{\Sigma k_B T}{\sqrt{2\pi\bar{m}H}} \quad (\text{B8})$$

where k_B is Boltzmann's constant, T is the disc temperature, $H = c_s/\Omega_K$ is the disc scale height, $c_s = \sqrt{k_B T/\bar{m}}$ is the gas sound speed, and \bar{m} is the mean molecular weight. Then

$$\frac{\partial \dot{M}_{\text{wind}}}{\partial r} = \frac{\sqrt{8\pi k_B} T}{\beta_0 \bar{m}} \frac{\mu \Sigma}{H \omega} = \frac{\sqrt{8\pi k_B}}{\sqrt{\bar{m}}\beta_0} T^{1/2} \mu \Sigma. \quad (\text{B9})$$

Combine (B9) and (B4) to find

$$u_r = -\sqrt{\frac{8}{\pi}} \frac{\sqrt{k_B}}{\sqrt{\bar{m}}\beta_0} T^{1/2} \mu(\lambda - 1) \sim -\frac{\mu(\lambda - 1)}{\beta_0} c_s. \quad (\text{B10})$$

In the fiducial model of Bai (2016, see their fig. 2), μ increases from ~ 0.06 at $r = 0.3$ AU to ~ 4 at 30 AU, and $(\lambda - 1)$ decreases from ~ 30 to ~ 2 over the same range; therefore the product $\mu(\lambda - 1)$ increases from ~ 2 to ~ 8 , scaling roughly as $r^{0.3}$. Their model temperature scales as $T \propto r^{-1/2}$; therefore the combination $T^{1/2}\mu(\lambda - 1)$ is nearly constant with r . Assuming it to be constant implies from (B10) that u_r is similarly constant (cf. Kimmig et al. 2020), if β_0 is constant:

$$u_r \sim -4 \left(\frac{10^5}{\beta_0} \right) \text{cm/s}. \quad (\text{B11})$$

Taking β_0 to be a strict constant corresponds to a model intermediate between the conserved-flux model of Bai (2016) (dashed line in the right panel of their fig. 5) and their flux-proportional-to-mass model (solid line). Using their initial fiducial $\beta_0 = 10^5$ implies the disc at $r = 30$ AU drains out in $r/|u_r| \simeq 3$ Myr.

This paper has been typeset from a $\text{\TeX}/\text{\LaTeX}$ file prepared by the author.